Original Article

Chemical power for microscopic robots in capillaries

Tad Hogg, PhD[a],*, Robert A. Freitas Jr, JD[b]

[a]*Hewlett-Packard Laboratories, Palo Alto, California, USA*
[b]*Institute for Molecular Manufacturing, Palo Alto, California, USA*

Abstract

The power available to microscopic robots (nanorobots) that oxidize bloodstream glucose while aggregated in circumferential rings on capillary walls is evaluated with a numerical model using axial symmetry and time-averaged release of oxygen from passing red blood cells. Robots about 1 μm in size can produce up to several tens of picowatts, in steady state, if they fully use oxygen reaching their surface from the blood plasma. Robots with pumps and tanks for onboard oxygen storage could collect oxygen to support burst power demands two to three orders of magnitude larger. We evaluate effects of oxygen depletion and local heating on surrounding tissue. These results give the power constraints when robots rely entirely on ambient available oxygen and identify aspects of the robot design significantly affecting available power. More generally, our numerical model provides an approach to evaluating robot design choices for nanomedicine treatments in and near capillaries.
© 2010 Published by Elsevier Inc.

Key words: Capillary; Nanomedicine; Nanorobot; Nanorobotics; Numerical model; Oxygen transport; Power

Implanted or ingested medical devices can gather diagnostic information and fine-tune treatments continually over an extended period of time, in contrast with the limited monitoring of a series of conventional laboratory tests. Current examples include pill-sized cameras to view the digestive tract as well as implanted glucose and bone-growth monitors to aid treatment of diabetes and joint replacements, respectively. Ongoing development of micromachines is significantly extending the capabilities of implanted devices, including stand-alone millimeter-scale microrobots for near-term in vivo surgical use. For example, external magnetic fields from a clinical magnetic resonance imaging (MRI) system can move microrobots containing ferromagnetic particles through blood vessels.[1-4] Other demonstrated micromachines use flagellar motors to move through fluids and offer the possibility of minimally invasive microsurgeries in parts of the body beyond the reach of existing catheter technology.[5,6]

Continuing the development of in vivo machines, nanotechnology has the potential to revolutionize health care[7-10] with devices small enough to reach and interact with individual cells of the body. Current efforts focus on nanomaterials to enhance diagnostic imaging and targeted drug delivery. For example, nanoparticles can target specific cell types for imaging or drug delivery.[11-14] Other efforts focus on developing more complex devices, such as multicomponent nanodevices called tectodendrimers, which have a single core dendrimer to which additional dendrimer modules of different types are affixed, each type designed to perform a function necessary to a smart therapeutic nanodevice.[15-17] These particles can also provide external control of some chemistry within cells, such as through tiny radiofrequency (RF) antennas attached to deoxyribonucleic acid (DNA) to control hybridization.

Further capabilities arise from combining the precision of these nanoscale devices with the programmability currently only available in larger machines. Such microscopic robots ("nanorobots"), with size comparable to cells, could provide significant medical benefits.[7,18-22] Realizing these benefits requires fabricating the robots cheaply and in large numbers. One approach to creating such robots is the engineering of biological systems (eg, RNA-based logic inside cells,[23] bacteria attached to nanoparticles,[24] executing simple programs via the genetic machinery within bacteria,[25,26] and DNA computers

responding to logical combinations of chemicals[27]). Another approach to manufacturing nanorobots is synthetic inorganic machines.[19] Such fabrication is beyond current technology but could result from ongoing progress in developing nanoscale devices. In particular, these machines could arise from continued development from currently demonstrated nanoscale electronics, sensors and motors,[28-36] and rely on directed assembly.[37]

A key benefit of micrometer-scale machines is they can pass through even the smallest vessels of the circulatory system and thereby can approach within a few cell diameters of most tissue cells of the body. However, this small size limits the capabilities of individual robots. For tasks requiring greater capabilities in conjunction with accessing individual cells, nanorobots could use the circulation to reach the desired locations and, once there, form aggregates by using self-assembly protocols.[19] For robots reaching tissues through the circulation, the simplest aggregates are formed on the inner wall of the vessel. Robots could also aggregate in tissue spaces outside small blood vessels by exiting capillaries via diapedesis,[19] a process similar to that used by immune cells.[38]

Aggregates of robots in one location for an extended period of time could be useful in a variety of tasks. For example, they could improve diagnosis by combining multiple measurements of chemicals.[39] Using these measurements, the aggregate could give precise temporal and spatial control of drug release[19,20] as an extension of an in vitro demonstration using DNA computers.[27] Using chemical signals, the robots could affect behavior of nearby tissue cells. For such communication, molecules on the robot's surface could mimic existing signaling molecules to bind to receptors on the cell surface.[19,40] Examples include activating nerve cells[41] and initiating immune response,[40] which could in turn amplify the actions of robots by recruiting cells to aid in the treatment. Such actions would be a small-scale analog of robots affecting self-organized behavior of groups of organisms.[42] Aggregates could also monitor processes that take place over long periods of time, such as electrical activity (eg, from nearby nerve cells), thereby extending capabilities of devices tethered to nanowires introduced through the circulatory system.[43] In these cases, the robots will likely need to remain on station for tens of minutes to a few hours or even longer.

The aggregate itself could be part of the treatment by providing structural support (eg, in rapid response to injured blood vessels[44]). Aggregates could perform precise microsurgery at the scale of individual cells, extending surgical capabilities of simpler nanoscale devices.[45] Because biological processes often involve activities at molecular, cell, tissue, and organ levels, such microsurgery could complement conventional surgery at larger scales. For instance, a few millimeter-scale manipulators, built from micromachine (microelectromechanical system; MEMS) technology, and a population of microscopic devices could act simultaneously at tissue and cellular size scales (eg, for diagnosis[46] or nerve repair[47,48]).

A major challenge for nanorobots arises from the physics of their microenvironments, which differ in several significant respects from today's larger robots. First, the robots will often operate in fluids containing many moving objects, such as cells, dominated by viscous forces. Second, thermal noise is a significant source of sensor error, and Brownian motion limits the ability to follow precisely specified paths. Finally, power significantly constrains the robots,[49,50] especially for long-term applications where robots may passively monitor for specific rare conditions (eg, injury or infection) and must respond rapidly when those conditions occur.

For medical tasks of limited duration, onboard fuel created during robot manufacture could suffice. Otherwise, the robots need energy drawn from their environment, such as converting externally generated vibrations to electricity[51] or chemical generators.[19] Power and a coarse level of control can be combined by using an external source (eg, light) to activate chemicals in the fluid to power the machines in specific locations,[52] similar to nanoparticle activation during photodynamic therapy,[53] or by using localized thermal, acoustic, or chemical demarcation.[19]

This article examines generating power for long-term robot activity from reacting glucose and oxygen, which are both available in the blood. Such a power source is analogous to bacteria-based fuel cells whose enzymes enable full oxidation of glucose.[54-56] We describe a computationally feasible model incorporating aspects of microenvironments with significant effect on robot performance but not previously considered in robot designs (eg, kinetic time constants determining how rapidly chemical concentrations adjust to robot operations). As a specific scenario, we focus on modest numbers of robots aggregated in capillaries.

A second question we consider is how the robots affect surrounding tissue. Locally, the robots compete for oxygen with the tissue and also physically block diffusion out of the capillary. Robot power generation results in waste heat, which could locally heat the tissue. The robot oxygen consumption could also have longer-range effects by depleting oxygen carried in passing red blood cells.

In the remainder of this article, we present a model of the key physical properties relevant to power generation for robots using oxygen and glucose in the blood plasma. Using this model, we then evaluate the steady-state power-generation capabilities of aggregated robots and how they influence surrounding tissue.

Methods

We consider microscopic robots using oxygen and glucose available in blood plasma as the robots' power source. This scenario involves fluid flow, chemical diffusion, power generation from reacting chemicals, and waste heat production. Except for the simplest geometries, behaviors must be computed numerically (eg, via the finite element method[57]).

This section describes our model. The simplifying approximations are similar to those used in biophysical models of microscopic environments, such as oxygen transport in small blood vessels with diffusion into surrounding tissue.[58,59] We focus on steady-state behavior indicating long-term robot performance when averaged over short-term changes in the local environment such as individual blood cells (exclusively erythrocytes, not white cells or platelets unless noted otherwise) passing the robots.
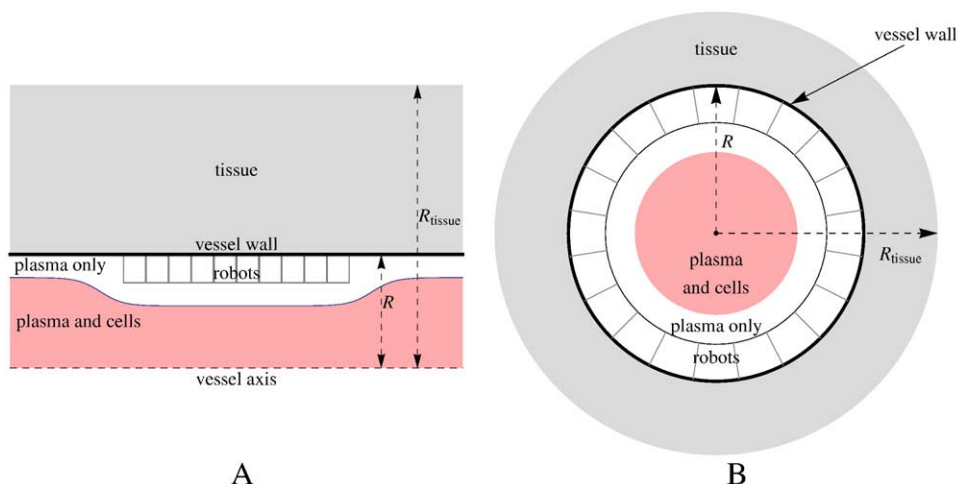
Figure 1. Schematic geometry of vessel, robots, and surrounding tissue. The relative sizes of the regions are not to scale for the parameters of our model (described in the section "Model parameters"). **(A)** A slice through the axially symmetric geometry with the vessel axis at the bottom, showing a cross section of 10 rings of robots. Fluid flows through the vessel from left to right, with varying speed depending on distance to the vessel wall. **(B)** Vessel cross section at the position of one ring of robots.

Blood vessel and robot geometry

Evaluating behavior in general three-dimensional geometries is computationally intensive. Simplified physical models give useful insight with significantly reduced computational requirements.[59] Such simplifications include using two-dimensional and axially symmetric three-dimensional geometries. The latter case, appropriate for behavior within vessels, has physical properties independent of angle of rotation around the vessel axis. We adopt this approach and consider the axially symmetric geometry illustrated in Figure 1: a segment of a small vessel with robots forming one or more rings around the vessel wall. The figure includes the Fahraeus effect: confinement of blood cells near the center of the vessel. The section "Effects of cells on flow and chemical transport" of this article describes how we model this effect.

To ensure axial symmetry, we model the robot's interior with uniform physical properties and take their shapes conforming to the vessel wall with no gaps between neighboring robots.[19] Thus, as seen in Figure 1, *B*, the surfaces of the robots contacting the plasma or the vessel wall are curved, so the robots are only roughly cubical. The other robot surfaces indicated in Figure 1 are not treated explicitly in our model.

Physically uniform robot interiors are convenient but not necessary for this model. An axially symmetric model only requires the robots to be uniform in the direction around the vessel and that the radial boundary surfaces between robots are treated as continuous with the interiors. Robot characteristics could vary in the direction along the vessel axis or radially. For example, the axially symmetric model could apply to robots whose power generators are close to the plasma-contacting surface to minimize internal oxygen transport, analogous to clumping of mitochondria in cells near capillaries.[59] Moreover, while we primarily focus on physically adjacent rings of robots, axial symmetry also holds for sets of rings that are spaced apart from each other along the vessel. We refer to a set of rings of robots as a *ringset*.

We ignore pulsatile variations in vessel circumference as these are mostly confined to the larger arterial vessels.[60] Thus, our model geometry is both axially symmetric and static.

Fluid flow

Viscosity dominates the motion of microscopic objects in fluids, producing different physical behaviors than for larger organisms and robots in fluids.[61-65] The Navier-Stokes equation describes the flow.[64,66] For the vessel geometry of Figure 1, the pressure difference between the inlet and outlet of the vessel determines the nature of the flow. We specify the pressure difference as ∇pL where ∇p is the overall pressure gradient and L is the length of the modeled segment of the vessel. Whereas some fluid leaks into or out of capillaries, we ignore this small component of the flow, in common with other models of blood flow in capillaries.[59,67] In our scenario, the robots are attached to the vessel wall. For modeling fluid behavior, such static robots merely change the shape of the vessel boundary. We apply the "no slip" boundary condition on both the robots and the vessel wall (ie, fluid speed is zero at these boundaries). Thus, the flow speed varies from zero at the wall to a maximum value in the center of the vessel.

Chemical diffusion

Microscopic robots and bacteria face similar physical constraints in obtaining chemicals.[68] At small scales, diffusion arising from random thermal motions is the main process transporting chemicals. Even at the scale of these robots, individual molecules and their distances between successive collisions are tiny. Thus, chemicals in the fluid are well approximated by a continuous concentration C specifying the number of molecules per unit volume. The concentration obeys the diffusion equation,[69]

$$\frac{\partial C}{\partial t} = -\nabla \cdot \mathbf{F} + \Gamma \tag{1}$$

where $\mathbf{F} = -D\nabla C + \mathbf{v}C$ is the chemical flux, ∇C is the concentration gradient, $\mathbf{v}$ is the fluid velocity vector, D is the chemical diffusion coefficient, and Γ is the reaction rate density (ie, rate at which molecules are created by chemical reactions per unit volume). The first term in the flux is diffusion, which acts to reduce concentration gradients, and the second term arises from movement of the fluid in which the chemical is dissolved.

Small molecules such as oxygen and glucose readily diffuse from capillaries into surrounding tissue. Eq. (1) also describes the transport within the tissues wherein $\mathbf{v} \approx 0$ (ie, the transport is completely due to diffusion). The diffusion coefficient of oxygen in tissue is close to that in plasma,[58] and for simplicity we use the same diffusion coefficients in both regions.

Kinetics of oxygen release from red blood cells

As robots consume oxygen from the plasma, passing red blood cells respond to the reduced concentration by releasing oxygen. An important issue for powering robots is how rapidly cells replenish the oxygen in the plasma as the cells pass the robots.

A key value determining the oxygen release from red blood cells is the hemoglobin saturation S: the fraction of hemoglobin capacity in a cell which has bound oxygen.[70] The oxygen concentration in the cell is $C_{O_2}^{max}S$, where $C_{O_2}^{max}$ is the concentration in the cell when all the hemoglobin has bound oxygen.

The saturation is high when the cell is in fluid with high oxygen content (ie, in the lungs) and low after the cell has delivered oxygen to tissues of the body. Quantitatively, the equilibrium saturation, conventionally expressed in terms of the equivalent partial pressure p of oxygen (O_2) in the fluid around the cell, is well described by the Hill equation[59]:

$$S_{equib}(a) = \frac{a^n}{1 + a^n} \tag{2}$$

where $a = p/p_{50}$ is the partial pressure ratio, p_{50} is the partial pressure at which half the hemoglobin is bound to oxygen, and n characterizes the steepness of the change from low to high saturation. The saturation in small blood vessels ranges from near 1 within the lungs to around one-third within working tissues. Henry's law relates the partial pressure to the concentration: $p = H_{o_2}C_{o_2}$ with the proportionality constant H_{O_2} depending on the fluid temperature.

Eq. (2) gives the equilibrium saturation (ie, the value in a red cell after residing a sufficiently long time in a fluid with partial pressure p). However, small robots consuming oxygen from the plasma may produce large gradients in oxygen concentration. If the oxygen concentration gradients and flow speed are high enough, passing cells will not have time to equilibrate with the abruptly decreased oxygen concentration before the flow moves them past the robots. Whether this is the case depends on the kinetics (ie, how rapidly cells change their saturation level when exposed to concentration changes). The timescale for oxygen release is determined by reaction kinetics of oxygen binding to hemoglobin in the cell and diffusion of these chemicals within the cell.

One model of this kinetics is a lumped-model differential equation relating saturation to concentration outside the cell.[71] In this model, the change in S, and hence the flux of oxygen from a cell into the surrounding plasma, is determined from the partial pressure ratio a as

$$\frac{dS(t)}{dt} = -\frac{1}{t_u}\sqrt{s(a, S(t))} \tag{3}$$

where t_u is a characteristic timescale for oxygen unloading, and the saturation unloading function s is

$$s(a, S) = \frac{2(1 - S)}{n + 1}a^{n+1} - 2Sa + \frac{2n}{n + 1}\frac{S^{1 + 1/n}}{(1 - S)^{1/n}}. \tag{4}$$

If oxygen partial pressure, p, varies over the surface of the cell, the rate of change is the average of the right-hand-side of Eq. (3) over the surface of the cell. Eq. (3) is consistent with the equilibrium relation of Eq. (2) because $s(a, S_{equib}(a)) = 0$.

As a boundary condition on oxygen saturation S, at the vessel inlet we take S equal to the equilibrium value with the oxygen plasma concentration specified at the inlet. Numerical evaluation of Eq. (3) requires care to accurately evaluate s when the concentration is close to equilibrium to avoid numerical instability if the computed concentration in the plasma is even slightly above the cell saturation.

The blood cells also have a role in removing the carbon dioxide (CO_2) produced by the robots (described in the following section). Only a small portion is transported dissolved in the plasma. Instead, most CO_2 is transported or chemically converted to bicarbonate within red cells. The detailed kinetics of these processes[72] does not directly limit robot power production and thus is beyond the scope of this article. Moreover, the robot power production rates considered here increase the carbon dioxide concentration by only a few percent, which can be buffered by processes within the passing cells and so is not likely to be a safety constraint on the power levels in the scenarios we consider.

Robot power generation

The overall chemical reaction combining glucose ($C_6H_{12}O_6$) and oxygen to produce water (H_2O) and carbon dioxide is

$$C_6H_{12}O_6 + 6O_2 \rightarrow 6CO_2 + 6H_2O.$$
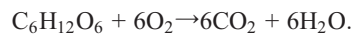
We denote the energy released by each such reaction by e. A robot absorbing oxygen molecules at a rate J_{O_2} produces power $J_{O_2}e/6$ because each reaction uses six O_2 molecules.

We consider robots on the vessel wall absorbing chemicals from the fluid only on their plasma-facing sides. For generating power with oxygen and glucose from the blood, oxygen is the limiting chemical.[19] We examine two design choices for the robots: how they collect oxygen arriving at their surface and their capacity for processing that oxygen to produce power.

For the first design choice, oxygen transport within the robots, we examine two extremes. In the basic ("no pumps") design, the robots absorb oxygen passively via diffusion. In the advanced ("with pumps") design, the robots use pumps on their surfaces to actively absorb all arriving oxygen and distribute this

gas to internal power-generating sites. We treat the full surface as available to absorb chemicals. In practice, robots will absorb chemicals with only a fraction of their surface. This is not a significant constraint for microscopic robots as even a modest fraction of a surface with absorbing sites gives absorption almost as large as that of a fully absorbing surface.[68]

For the second design choice, robot power production capacity, we also examine two cases. Onboard generating capacity arises from the number and efficiency of the internal reaction sites (eg, fuel cells)[19,54,56] in each robot. If capacity is constrained by engineering feasibility of fuel cell fabrication or by difficulty of placement into the robots, the robots will have relatively few fuel cells—and consequently a low maximum capacity for power generation—hence are called "low-capacity" robots. When these constraints do not apply, we have "high-capacity" robots.

A robot with sufficient pump and generating capacity produces power from all oxygen reaching the robot. This oxygen-limited situation corresponds with a zero-concentration boundary condition for the oxygen concentration in the fluid at the robot surface. With this boundary condition, integrating the dot product of the flux $\mathbf{F}$ (determined from Eq. (1)) and normal vector of the plasma-facing surface of the robot gives the rate J_{O_2} (molecules per unit time) at which the robot absorbs oxygen molecules, with no need to explicitly model oxygen transport and consumption inside the robot. Whereas pumps cannot maintain the zero-concentration boundary condition at arbitrarily high oxygen flux, theoretical pump capacity appears more than adequate for the oxygen concentrations relevant to our model.[19]

A robot's power-generating capacity is limited by the number of reaction sites it contains, N_{react}, and by the maximum rate of reacting glucose and oxygen at each site, r. Specifically, the steady-state oxygen absorption rate must satisfy $J_{O_2} \leq 6N_{react}r$. If this bound on absorption rate is smaller than the oxygen flux corresponding with the zero-concentration boundary condition the pumps could maintain, then the robot's power generation will be capacity-limited rather than oxygen-limited, and the zero-concentration boundary condition will not apply. In this situation, for a robot with pumps, we consider the pumps delivering as much oxygen as the reaction sites can process, giving robot power generation equal to its maximum possible value, namely, $N_{react}re$.

Determining power generation for robots without pumps requires explicitly modeling the oxygen transport and power generation within the robot. In this case, the oxygen moves by diffusion within the robot. We treat power generation as spatially continuous rather than occurring at discrete reaction sites, thereby maintaining axial symmetry. Thus, Eq. Eq. (1) applies within the robot, with the reaction rate density for oxygen, Γ, determined by the number density of reaction sites, ρ_{react}, and the reaction kinetics of each site. For uniformly distributed reaction sites, $\rho_{react} = N_{react}/V_{robot}$ where V_{robot} is the volume of each robot. Specifically, at a given location inside the robot, $\Gamma = 6P_{robot}/e$ where P_{robot} is the power-generation density (ie, the power generated per unit volume at that location). We model robot power generation using Michaelis-Menten kinetics[73] assuming oxygen is the limiting factor because glucose

concentrations are typically two orders of magnitude larger than those of oxygen[19]:

$$P_{robot} = e\rho_{react}r\frac{C_{O_2}}{K + C_{O_2}} \tag{5}$$

where K is the concentration of O_2 giving half the maximum reaction rate. The total power generated by a robot is the integral of P_{robot} over the robot's volume, which is the same as the power determined from the rate the robot absorbs oxygen (ie, $eJ_{O_2} / 6$). In this no-pumps case, J_{O_2} is determined from the solution of Eq. (1) in the fluid and robot interior rather than from a boundary condition on the robot's surface.

The number of reaction sites in a robot is a design choice, limited by the volume of each reaction site. As an example, a nanoscale oxygen-glucose fuel cell could be as small as 3000 nm^3 with $r = 10^6$ glucose molecules per second.[19] ρ_{react} cannot be larger than the reciprocal of this volume—which would correspond with the robot entirely filled by power-generation reaction sites. To illustrate the trade-offs among these design choices, we consider high- and low-capacity robots, both with and without pumps. Increasing oxygen concentration at the reaction sites increases their power output closer to their maximum (as the fraction appearing in Eq. (5) gets closer to its maximum value of 1). Thus, pumps can at least somewhat compensate for a decrease in the number of functional reaction sites by increasing the oxygen concentration so the remaining reaction sites operate more efficiently. On the other hand, if pumps are more difficult to fabricate than fuel cells, robots would benefit from a large number of fuel cells (high capacity) to compensate for the inability of passive diffusion to increase concentrations. As another approach to dealing with few fuel cells, we also consider placing all of them near the plasma-facing surface of the robot, where oxygen concentration is highest in the passive diffusion (no-pumps) design.

Oxygen use in tissues

Models of oxygen use and power generation in tissues can include various details of tissue structure.[59] A simple approach, adopted in this article, treats the tissue surrounding the vessel as homogeneous and metabolizing oxygen (assumed to be the rate-limiting chemical) with kinetics similar in form to Eq. (5):

$$P_{tissue} = P_{tissue}^{max}\frac{C_{O_2}}{K + C_{O_2}} \tag{6}$$

where P_{tissue}^{max} is the power demand (power per unit volume) of the tissue, and K_{tissue} is the concentration of O_2 giving half the maximum reaction rate.

Heating

The robot-generated power eventually dissipates as waste heat into the environment. Heat transfer from the robots to their surroundings occurs by both conduction and convection due to the moving fluid. We take the tissue environment outside the vessel to be small enough so as not to include other vessels. Thus heat transport in the tissue is via conduction only.

The temperature T obeys a version of Eq. (1)[66]:

$$\rho c_{\text{thermal}} \frac{\partial T}{\partial t} = -\nabla \cdot \mathbf{F} + Q \tag{7}$$

where $\mathbf{F} = -k_{\text{thermal}}\nabla T + \rho c_{\text{thermal}} T \mathbf{v}$ is the heat flux, ∇T is the temperature gradient, $\mathbf{v}$ is the fluid velocity vector, ρ is fluid density, k_{thermal} is the fluid's thermal conductivity, c_{thermal} is the fluid's heat capacity, and Q is the heat generation rate density, which is the same as the power production per unit volume. For robots absorbing all oxygen reaching them (ie, using pumps), we take Q uniform within the robot, that is, equal to $eJ_{O_2}/(6V_{\text{robot}})$. For robots without pumps, power generation varies within the robot, with $Q = P_{\text{robot}}$ from Eq. (5). For temperature boundary conditions, we take the incoming fluid and the outermost radius of the tissue cylinder to be held at body temperature.

While we could include tissue power generation as a heat source in the heat equation, here we focus on the additional heat from the robots alone. Thus we evaluate how robot power generation adds to the heat load produced by the tissue. We do not consider any changes in the tissue, either locally or systemically (eg, increasing blood flow), in response to the additional heating. This is a reasonable assumption given the tiny temperature increase described in the section "Tissue power and heating".

Effects of cells on flow and chemical transport

In small blood vessels, individual blood cells are comparable in size to the vessel diameter. Thus, at the length scales relevant for microscopic robots, the fluid consists of plasma separating relatively large objects. The cells significantly affect the fluid flow and, because cells are not rigid, the flow alters the shape of the cells (though we can ignore red blood cell rotation-induced elevation of diffusivity[74] because these cells are motionally restricted in capillaries and elevation is lowest for small molecules such as O_2). Similarly, the vessel walls are not rigid, which somewhat changes both the flow and the vessel boundary. A key consequence for oxygen transport is the confinement of cells toward the center of the vessel. The cell-free fluid near the vessel wall is a gap over which oxygen released by cells must diffuse to reach the vessel wall or the plasma-facing robot surface. In capillaries, this gap ranges from about 0.5 to 1 μm, depending on flow speed.[67,75]

Modeling the interactions between fluid and blood cells is computationally feasible for a few cells in capillaries.[70,76] However, modeling interactions with many deforming cells is challenging, and close packing of objects moving in fluid leads to complex hydrodynamic interactions.[77,78] Instead of evaluating these effects in detail, we use approximate models that average over the cell behaviors and assume rigid vessel walls. Such models are commonly used to study oxygen delivery in tissue.[59] This averaging approach also simplifies analysis of collective robot behavior.[79-81]

In this approximation, the vessel only contains fluid, which consists of two components as illustrated in Figure 1. The first component models the mix of cells and plasma in the central portion of the vessel. Instead of explicitly modeling individual cells, this approximation averages over the cell positions in the

fluid. The second component is the fluid near the vessel wall, consisting of plasma only.

The fluid component modeling the mix of cells and plasma is confined to a distance R_{cell} from the vessel axis. This distance varies with position along the vessel, as shown in Figure 1, because robots on the wall reduce the volume available to the passing fluid. Thus, all oxygen released by the passing cells is within a distance R_{cell} of the vessel axis, and this oxygen must diffuse through the plasma gap to reach the robots or the tissue. We take R_{cell} to follow a fluid streamline with the gap appropriate for the fluid speed in the section of the vessel far from the robots.[75] This approximation accounts for the location of cells toward the center of the vessel without the complexity of modeling how cells change shape as they pass the robots.

A key parameter for oxygen delivery is the hematocrit, h_{full} (ie, the fraction of the capillary volume occupied by cells). In our model, the more relevant parameter is the hematocrit, h, within the fluid component containing the cells, which has a smaller volume than the full vessel. As both values must give the same rate for cells passing through the vessel, these quantities are related by

$$h = h_{\text{full}} \frac{R^2 v_{\text{avg}}}{R_{\text{cell}}^2 v_{\text{cell}}} \tag{8}$$

where v_{avg} is the average flow speed in the vessel, and v_{cell} is the average flow speed within the central portion of the vessel with fluid component modeling the cells. Fluid speed is faster near the center of the vessel than near the walls, so v_{cell} is larger than v_{avg}. The quantities v_{avg}, v_{cell}, and R_{cell} vary along the length of the vessel, but the ratio appearing in Eq. (8) is constant due to our choice of R_{cell} following a fluid flow streamline. Within the cell fluid component, oxygen bound to hemoglobin has concentration $hC_{O_2}^{\text{max}}S$, and oxygen in the plasma has concentration $(1-h)C_{O_2}$. Future evaluations of the accuracy of this simplifying approach to oxygen delivery might include results from more detailed models comparing oxygen release from red cells with that of hemoglobin-based oxygen carriers dissolved in plasma rather than contained in cells.[82] This averaging over cell position can also be viewed as approximating the time-averaged behavior as cells pass the robots on the vessel wall.

We model the kinetics of oxygen release from passing cells as due to changes in cell saturation in the cell fluid component (ie, S). The effect of oxygen release from red cells into the plasma arises from the rate of change in saturation inside the cells,[71] as discussed in the section "Kinetics of oxygen release from red blood cells" with Eq. (3). Thus the reaction term in Eq. (1) for oxygen in the fluid component with the cells is

$$\Gamma = -hC_{O_2}^{max} \frac{dS}{dt}. \tag{9}$$

Because dS/dt from Eq. (3) is negative, this value for Γ is positive, giving an increase in oxygen in the plasma.

We determine S along the vessel using the lumped model discussed in the section "Kinetics of oxygen release from red blood cells." The value of S along the vessel is governed by a one-dimensional version of the diffusion equation based on the

Table 1
Model parameters for fluid, vessel, and tissue*

Parameter	Value
Geometry	
Vessel radius	$R = 4$ μm
Tissue cylinder radius	$R_{tissue} = 40$ μm
Modeled vessel length	$L = 100$ μm
Fluid	
Ambient temperature	$T = 310$ K
Thermal conductivity	$k_{thermal} = 0.6$ W m^{-1} K^{-1}
Heat capacity	$c_{thermal} = 4200$ J kg^{-1} K^{-1}
Fluid density	$\rho = 10^3$ kg/m^3
Fluid viscosity	$\eta = 10^{-3}$ kg m^{-1} s^{-1}
Pressure gradient	$\nabla p = 1 \times 10^5$ to 5×10^5 Pa/m
Hematocrit	$h_{full} = 25\%$
Tissue	
Power demand	$P_{tissue}^{max} = 4$ to 60 kW/m^3
O$_2$ concentration for half power	$K_{tissue} = 10^{21}$ molecule/m^3
Reaction energy from one glucose molecule	$e = 4 \times 10^{-18}$ J
Density, thermal conductivity	Same as fluid
Red blood cells	
Partial pressure for 50% O$_2$ saturation	$p_{50} = 3500$ Pa
O$_2$ saturation exponent	$n = 2.7$
Time constant for O$_2$ unloading	$t_u = 76$ ms
Maximum O$_2$ concentration in cell	$C_{O_2}^{max} = 10^{25}$ molecule/m^3
Heme diffusion coefficient	$D_{heme} = 1.4 \times 10^{-11}$ m^2/s
Chemicals in plasma	
O$_2$ diffusion coefficient	$D_{o_2} = 2 \times 10^{-9}$ m^2/s
O$_2$ concentration at inlet	$C_{o_2} = 3 \times 10^{22}$ to 7×10^{22} molecule/m^3
O$_2$ partial pressure to concentration ratio	$H = 1.6 \times 10^{-19}$ Pa/(molecule/m^3)

  * We consider two values, the extremes of the listed range, for parameters indicated in boldface. For the vessel without robots, the pressure gradient range corresponds with average flow speeds of $v_{avg} = 0.2$ to 1 mm/s. The corresponding hematocrit values within the cell fluid component are $h = 0.31$ to 0.36. See text for source references.

average flow speed in the cell fluid component, v_{cell}, and using the chemical diffusion coefficient for oxygen bound to hemoglobin in the cell, D_{heme}. We determine the reaction term in the diffusion equation for S, for each position along the vessel, by averaging the right-hand side of Eq. (3) over the cross section of the vessel at that position, based on the oxygen concentration in the plasma of the plasma and cell component of the fluid. This average value gives the rate of change for the saturation of cells as they pass that position along the vessel. In this way, the changes in saturation within the cells and the concentration in the plasma are coupled equations that are solved simultaneously.

Model parameters

Table 1 lists the parameter values we use. To locate the boundary between the fluid component modeling the cells and the cell-free component near the vessel wall, we use cell-free gaps of 0.98 and 1.27 μm at the vessel inlet for pressure gradients of 10^5 and 5×10^5 Pa/m, respectively. For the 10-μm ringset, the fluid streamline becomes nearly flat (ie, fluid velocity in the radial direction is nearly zero) near the middle of the aggregate, and the corresponding cell-free gap for the narrow section of the vessel by the robots (ie, of radius 3 μm) matches that for a long vessel with radius 3 μm.[75]

Table 2
Two scenarios: low with low tissue power demand (basal rate) and slow fluid flow, and high with high tissue power demand and fast fluid flow*

Parameter	Scenario	
	Low demand	High demand
Pressure gradient	$\nabla p = 10^5$ Pa/m	$\nabla p = 5 \times 10^5$ Pa/m
Tissue power demand	$P_{tissue}^{max} = 4$ kW/m^3	$P_{tissue}^{max} = 60$ kW/m^3

  * Both scenarios use high inlet concentration: $C_{O_2} = 7 \times 10^{22}$ molecule/m^3 (arterial).

We assume the fluid properties (ie, density, viscosity, heat capacity, and thermal conductivity) are uniform throughout the model and roughly equal to those of water. The pressure gradient range we consider corresponds with average flow speeds of 0.2 to 1 mm/s in a vessel of radius R without robots. These speeds are typical of measured flow in capillaries.[19] For comparing vessels with and without robots, we use the same pressure gradients in both cases. That is, we compare constant-pressure boundary conditions rather than constant-velocity conditions. The ambient temperature is body temperature, and the hematocrit value is typical of small blood vessels,[19] which is somewhat lower than in larger vessels.

For the kinetics, K_{tissue} is from Ref. [58] and the blood cell kinetics parameters are from Refs. [71] and [59]. The oxygen concentration range corresponds with venous and arterial ends of capillaries.[19] Concentrations of glucose and CO_2 in blood plasma are in the millimolar range (about 10^{24} molecule/m^3), far larger than the oxygen concentrations.[19] For evaluating microscopic robot behavior, a convenient measure of chemical concentration in a fluid is number of molecules per unit volume. Much of the existing literature uses units convenient for larger scales, such as moles of chemical per liter of fluid (ie, molar, M) and grams of chemical per cubic centimeter. Discussions of gases dissolved in blood often specify concentration indirectly via the corresponding partial pressure of the gas under standard conditions. As an example, oxygen concentration $C_{o_2} = 10^{22}$ molecule/m^3 corresponds with a 17 μM solution, 0.53 μg/cm^3, and with a partial pressure of 1600 Pa or 12 mmHg.

Tissue power demands vary considerably, depending on the tissue type and overall activity level. We consider typical values of resting and high power demand[19] and focus on two extreme scenarios given in Table 2. The low-demand scenario is the likely situation for most medical procedures in practice. The high-demand scenario has a relatively high tissue demand but is not the peak metabolic rate in human tissue, which can reach rates as high as 200 kW/m^3.[58]

Fluid and chemical properties vary with temperature, but, as described below, the temperature range seen in our model is very small. Thus, we take the values at body temperature. We also treat the saturation curve of Eq. (4) as constant although it varies somewhat with CO_2 concentration through a change in p_{50}.

The robot size, number aggregated on the vessel wall, and power-generation capacity are design choices, with the values we consider given in Table 3. We consider sets of circumferential rings along the vessel wall either 1 or 10 adjacent robots long. These aggregates consist of 20 and 200 robots, respectively. We estimate K as the value corresponding with fuel cells based on

Table 3
Robot design parameters*

Parameter	Value
Geometry	
Robot size	$L_{robot} = 1$ μm
Robots per circumferential ring	20
Robot volume	$V_{robot} = 1.1$ μm^3
Length of aggregate	1 to 10 μm
Power generation	
Power generation site density	$\rho_{react} = 0.06 \times 10^{21}$/m^3 to 3×10^{21}/m^3
Power generation reaction rate	$r = 10^6$/s
O$_2$ concentration for half power	$K = 10^{24}$ molecule/m^3

  * The robot size is the length of each robot in the radial and longitudinal directions. The curved surfaces facing the plasma and vessel wall have slightly different lengths. When not limited by availability of oxygen or glucose, a power-generation reaction site produces $er = 4$ pW. We consider two values, the extremes of the listed range, for parameters indicated in boldface. The number of power-generation sites in each robot, $N_{react} = \rho_{react}V_{robot}$, ranges from 66 to 3300, with corresponding maximum power per robot, reN_{react}, of 260 pW and 13,000 pW for low- and high-capacity robots, respectively.

the glucose oxidase enzyme.[83] The high- and low-capacity robot designs correspond with the choices of reaction site density given in Table 3. For the high-capacity case, the power generation uses about 1% of the robot volume with the fuel cells described in the section "Robot power generation." As shown in the "Results" section, the maximum power generation, even for the low-capacity case, is considerably larger than possible with the available oxygen. So these design choices are reasonable for studying limitations due to available oxygen.

In our model, the fluid flow is independent of the chemical concentrations, and both are independent of the heat generation due to our assumption that the parameters of Table 1 are independent of temperature in the narrow physiologic range. This simplifies the numerical solution by allowing an iterative procedure: solving first for the fluid flow, then for the chemical concentration, and finally for the temperature. Specifically, we first solve for the fluid flow in the vessel as determined by the vessel and robot geometry and the imposed pressure gradient. Given the fluid velocity, we then simultaneously solve Eq. (1) for the oxygen concentration and Eq. (3) for the blood cell average oxygen saturation. Eq. (5) and Eq. (6) give the power-generation density in the robots and tissue, respectively. For robots with pumps, we impose the boundary conditions on the plasma-facing robot surface described in the section "Robot power generation" and do not need to solve Eq. (1) inside the robot. Dividing the power generation by $e/6$, where e is the energy per reaction, gives the corresponding oxygen reaction rate densities Γ appearing in Eq. (1) (ie, the number of oxygen molecules consumed per unit volume per unit time at each location). This solution gives the oxygen concentration C_{O_2} and flux $\mathbf{F}$ throughout the vessel and the tissue and the average cell saturation S as a function of distance along the vessel. Finally, solving Eq. (7) using the solutions for the fluid flow and power generated by the robots gives the temperature increase due to the robots. We solve for steady-state behaviors using the finite element method,[84] though the model also applies to time-dependent scenarios.

Results

Figure 2 shows the distribution of oxygen in the tissue and plasma in the vessel near the robots. The robots reduce the local oxygen concentration far more than the surrounding tissue, as seen by comparing with the vessel without robots. Most of the extra oxygen used by the robots comes from the passing blood cells, which have about 100 times the oxygen concentration of the plasma. Within the vessel with the robots, the concentration in the plasma is lowest in the fluid next to the robots. Downstream of the robots is a recovery region where the concentration increases a bit as cells respond to the abruptly lowered concentration near the robots. In the low-demand scenario, the concentration in the vessel just downstream of the robots is somewhat lower than in the surrounding tissue. Thus in this region, the net movement of oxygen is from the tissue into the vessel, where the fluid motion transports the oxygen somewhat downstream before it diffuses back into the tissue. In effect, part of the oxygen entering the vessel travels through the tissue around robots to the downstream section of the vessel, in contrast with the pattern without robots where oxygen is always moving from the vessel into the surrounding tissue. The streamlines in Figure 2 show that the laminar flow speeds up as the fluid passes through the narrower vessel section where the robots are stationed.

Figure 3 gives another view of how the robots affect the oxygen concentration in the surrounding tissue. The concentration is zero at the robot surface facing into the vessel. The robots decrease the oxygen concentration somewhat but do not affect tissue power generation much because the concentration remains well above the threshold where power generation drops significantly (ie, K_{tissue} given in Table 1). However, at large distances from the vessel in the high-demand scenario, oxygen concentration is low enough to significantly decrease tissue power production. This low level of oxygen also occurs when there are no robots.

Figure 3 includes comparison with the simpler Krogh model of oxygen transport to tissue from vessels without robots.[85] The Krogh model assumes constant power density in the tissue and no diffusion along the vessel direction in the tissue. For the low-demand scenario, the Krogh model results are close to those from our model. However, in the high-demand case, the Krogh model has oxygen concentration drop to zero about 10 μm from the vessel, due to the unrealistic assumption of constant power use rather than the decrease in power use at low concentrations given by Eq. (6).

Oxygen flux to the robots ranges from about 10^{19} to 10^{20} molecule m^{-2} s^{-1} with the zero-concentration boundary condition. Estimates of pump capabilities are up to 10^{22} molecule m^{-2} s^{-1},[19] which is more than 100 times the actual flux to the robots. Such pumps could thereby maintain the zero concentration boundary condition. At an energy use of 10^{-20} J/molecule,[19] the pumps would require about 1 pW per robot to handle the incoming flux, slightly reducing the power benefit of the pumps. However, much of this pumping energy may be recoverable by adding a generator using the subsequent expansion of the reaction products to their lower partial pressure outside the robot.[18]
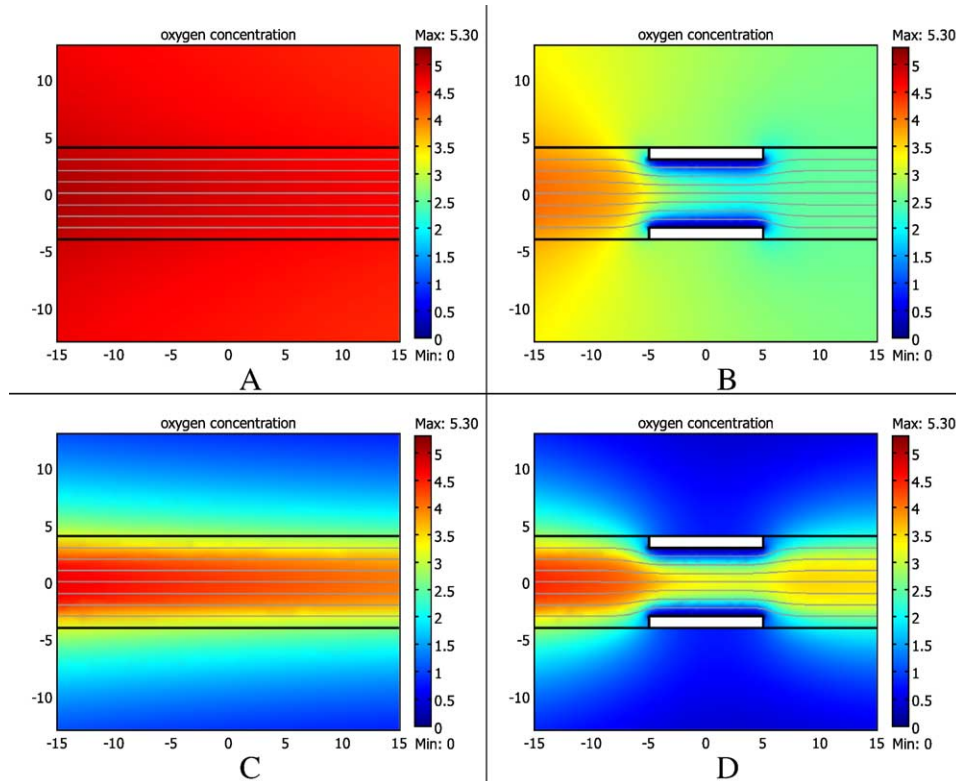
Figure 2. Oxygen concentration in the tissue and plasma within the vessel. Each diagram shows a cross section through the vessel and surrounding tissue of length 30 μm. Typically, this length of vessel contains about four cells. The left plots **(A, C)** are for the vessel without robots. The right plots **(B, D)** include the 10-μm ringset with pumps, which occupies the circumferential volume indicated by the white rectangles next to the vessel wall. The top and bottom plots are for the low- and high-demand scenarios of Table 2, respectively. Fluid in the vessel flows from left to right. Distances along the sides of each plot are indicated in micrometers, and concentrations on the color bars are in units of 10^{22} molecule/m³. The horizontal black lines are the vessel walls, and the gray curves inside the vessel are fluid flow streamlines.
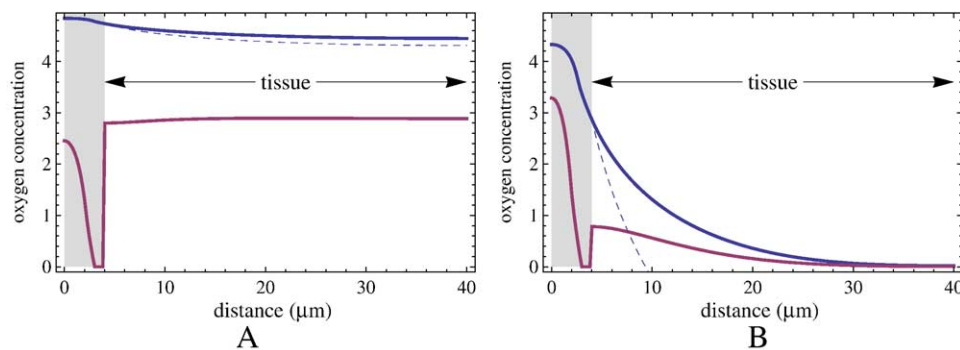

Figure 3. Oxygen concentration, in units of 10^{22} molecule/m³, along a radial cross section from the center of the vessel to the outer edge of the tissue region. The cross section is in the middle of the modeled section of vessel and tissue, corresponding with a vertical line in the center of each plot of Figure 2. The gray area indicates the interior of the vessel. In each plot, the upper curve is for the vessel without robots, and the lower curve is for the vessel containing the 10-μm ringset with pumps. For comparison, the dashed curves are solutions to the Krogh model[85] corresponding with the vessel without robots. **(A, B)** Low- and high-demand scenarios of Table 2, respectively.

Robot power

This section describes the steady-state power available to the robots according to our model in various scenarios. We first discuss the average per robot power in the aggregate, for both high- and low-capacity cases, which also indicates the total power available to the aggregate as a whole. We then show how the power is distributed among the robots, based on their location in the ringset.

Finally, we illustrate the qualitative features of these results in a simpler, analytically solvable model to identify key scaling relationships between robot design choices and power availability.

Average robot power

Table 4 gives the average power generated using the available oxygen, per robot within the aggregate. As expected, robots

Table 4
Average per-robot power generation (in picowatts) in various scenarios*

Robot power generation capacity	High capacity								Low capacity			
Inlet concentration C_{O_2} (10^{22}/m^3)	3	3	3	3	7	7	7	7	7	7	7	7
Pressure gradient ∇p (10^5 Pa/m)	1	1	5	5	1	1	5	5	1	1	5	5
Tissue power demand P_{tissue}^{max} (kW/m^3)	4	60	4	60	4	60	4	60	4	60	4	60
10-µm ringset (with pumps)	12	8	14	12	**17**	11	24	**18**	**17**	11	24	**18**
10-µm ringset (free diffusion)	11	7	12	10	**15**	10	22	**16**	**6**	3	8	**6**
1-µm ring (with pumps)	44	27	49	36	**69**	36	99	**58**	**69**	36	99	**58**
1-µm ring (free diffusion)	31	19	34	25	**49**	25	71	**38**	**9**	4	12	**7**

* Free diffusion is the "no pumps" case. The values in boldface correspond with the low- and high-demand scenarios of Table 2.

receive more oxygen and hence can generate more power when inlet concentration is high, fluid speed is high or tissue power demand is low. In the first two cases, the flow brings oxygen through the vessel more quickly; in the last case, surrounding tissue removes less oxygen. The less than twofold decrease in robot power generation in the face of a larger 2.5-fold decrease in O_2 inlet concentration from the arterial to the venous end of the capillary shows that robots extract more oxygen from red cells than these cells would normally release while passing the length of the vessel. Thus, robots get some of their oxygen as "new oxygen" rather than just taking it from what the tissues would normally get. This is possible because in this case, robots create steeper concentration gradients than the tissue does.

The 10-µm ringset with pumps produces about the same power in the low- and high-demand scenarios, consuming oxygen at 5×10^9 molecule/s.

Comparing the different aggregate sizes shows lower power generation, per robot, in the large aggregate compared with the small one. This arises from the competition among nearby robots for the oxygen. Nevertheless, the larger aggregate, with 10 times as many robots, generates several times as much power in aggregate as the smaller one. This difference identifies a design choice for aggregation: larger aggregates have more total power available but less on a per robot basis.

Robots using pumps generate only modestly more power than robots relying on diffusion alone in our high-capacity design example (see the "Robot power generation" section). In this case, for robots without pumps, the power-generation site density, ρ_{react}, is sufficiently large that oxygen molecules diffusing into the robot are mostly consumed by the power generators near the surface of the robot before they have a chance to diffuse back out of the robot. For such robots, power generators far from the plasma-facing surface receive very little oxygen and hence do not add significantly to the robot power production.

Pumps give higher benefit for isolated rings of robots than for tightly clustered aggregates. Although not evaluated in the axially symmetric model used here, pumps may be even more significant for a single isolated robot on the vessel wall. Such a robot would not be competing with any other robots for the available oxygen though would still compete with nearby tissue.

Low-capacity robots

The low-capacity robots have only 1/50th the maximum power-generating capability of the high-capacity robots discussed earlier. Nevertheless, each robot's maximum power is several times larger than the limit due to available oxygen. Thus, pumps allow the robots to produce the same power as given in Table 4 for the high-capacity robots. The pumps ensure the absorbed oxygen is completely used by the smaller number of reaction sites by increasing the concentration of oxygen within the robots, so Eq. (5) gives the same power generation in spite of the smaller value of ρ_{react}.

On the other hand, the smaller number of reaction sites is a significant limitation for robots without pumps. Comparing with Table 4 shows pumps improve the average power by factors of about 3 and 8 for the 10- and 1-µm ringsets, respectively. Comparing with high-capacity robots without pumps shows the factor of 50 reduction in reaction sites only reduces average power by factors of about 3 and 5 for the 10- and 1-µm ringsets, respectively. Thus, the reaction sites in the low-capacity scenario are used more effectively than in the high-capacity robots: With a smaller number of sites, each site does not compete as much with nearby sites for the available oxygen.

Much of the power in robots without pumps is generated near the plasma-facing surface, where oxygen concentration is largest. In our case, the power for the high-capacity robots is generated primarily within 100 nm of the robot surface. This observation suggests that a design with power-generating sites placed near this surface instead of uniformly throughout the robot volume, as we have assumed, could significantly improve power generation for robots without pumps. For example, placing all the reaction sites uniformly within the 1/50th of the robot volume nearest the surface would increase the local reaction site density in that volume by a factor of 50. For low-capacity robots, this placement would increase ρ_{react} to the same value as the high-capacity case, but only in a narrow volume, within 23 nm of the surface with the robot geometry we use. Elsewhere in the robot with this design $\rho_{react} = 0$. Whereas we might expect this concentration to increase power significantly, in fact we find only a small increase (eg, 12% for the 10-µm ringset in the low-demand scenario). Thus, concentrating the reaction sites near the plasma-facing surface does not offer much of a performance advantage.

Distribution of power among robots

Whereas all robots in a single ring have the same power due to the assumption of axial symmetry, Figure 4 shows that power varies with ring position in the 10-µm ringset. The robots at the upstream edge of the aggregate receive more oxygen than the other robots and hence produce more power. Power generation
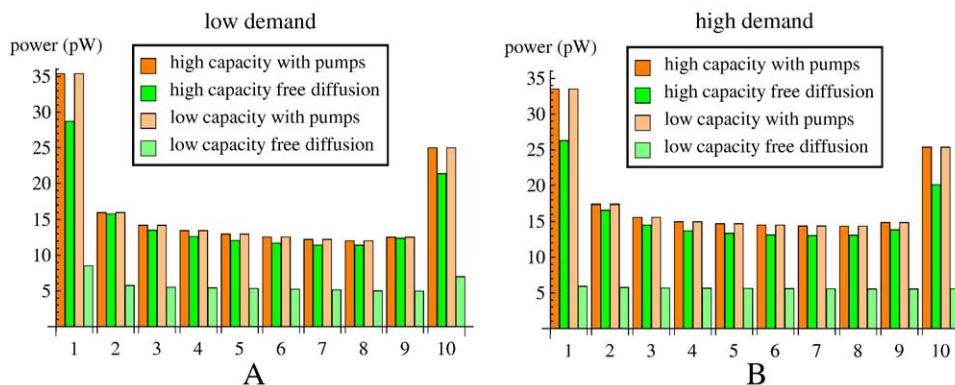
Figure 4. Steady-state power generation, in picowatts, for robots as a function of their position along the vessel wall, starting from those at the upstream end of the ringset (position 1) and continuing to those at the downstream end (position 10). The charts compare robots with pumps, absorbing all oxygen reaching them, with robots relying on free diffusion (ie, without pumps), and high- and low-capacity robots. For robots with pumps, power for high- and low-capacity cases are the same. **(A, B)** Low- and high-demand scenarios of Table 2, respectively.

does not decrease monotonically along the vessel: Robots at the downstream edge have somewhat more available oxygen than those in the middle of the aggregate as robots at the edge of the aggregate have less competition for oxygen. Figure 4 shows significantly larger benefits of pumps at the edges of multiring aggregates than in their middle sections, especially in the low-demand scenario.

In the scenarios described earlier, robots produce power from all the available oxygen. This is appropriate for applications requiring as much power as possible for the aggregate as a whole. At the other extreme, an application requiring the same behavior from all robots in the aggregate would be limited by the robots with the least available power. This would be the case for identical robots, all of which perform the same task and hence use the same power. In this case, the robots could increase performance by transferring power from those at the edges of the aggregate to those in the middle. Such transfer could take place after generation (eg, via shared electric current) or prior to generation by transfer of oxygen among neighboring robots. However, such internal transfer would require additional hardware capabilities. For robots with pumps, an alternative transfer method is for robots near the edge of the aggregate to run their pumps at lower capacity and thus avoid collecting all the oxygen arriving at their surfaces. This uncollected oxygen would then be available for other robots, though some of this oxygen would be transported by the fluid past the robots or be captured by the tissue rather than other robots. This approach increases power to robots in the middle of the aggregate without requiring additional hardware for internal transfers between robots, but at the cost of somewhat lower total power for the aggregate. Increasing as much as possible the power to the robots with the least power leads to a uniform distribution of power among the robots.

To quantify the trade-off between total power and its uniformity among the robots, we consider all robots setting each of the pumps on their surfaces to operate at the same rate and the pumps uniformly distributed over the surface. This gives a uniform flux of oxygen over the entire surface of all the robots. The largest possible value for this uniform flux, and hence the largest power for the aggregate, occurs when the minimum oxygen concentration on the robot surfaces is zero—at that point, the robot whose surface includes the location of zero concentration cannot further increase its uniform flux. For example, in the low-demand scenario, the maximum value for this uniform flux is approximately 2.22×10^{19} molecule m^{-2} s^{-1}. Compared with the situation in Figure 4, this uniform flux gives significantly lower power (39% leading ring, 56% trailing ring) for the robots at the edges of the aggregate, somewhat lower power for robots in positions 2 and 3 (87% and 98%, respectively), and somewhat more power (ranging from 104% to 116%) for the other robots. The combination of these changes gives a total of 84% of the power for the aggregate when every robot collects all the oxygen reaching its surface. The minimum power per robot increases from 12 pW to 14 pW. Robots could slightly increase power by accepting some nonuniformity of flux over each surface while maintaining the same total flux to each robot. This would occur when the minimum oxygen concentration on the entire length of the robot surfaces in a particular robot ring is zero.

Using this approach to uniform power in practice would require the robots to determine the maximum rate they can operate their pumps while achieving uniform power distribution. This rate would vary with tissue demand, and also over time as cells pass the robots. A simple control protocol is for each robot to adjust its pump rate up or down according to whether its power generation is below or above that of its neighbors, respectively. When concentration reaches zero on one robot, increasing pump rate at that location would not increase power generation. Communicating information for this protocol is likely simpler than the hardware required to internally transfer power or oxygen among robots but also requires that each robot is able to measure its power-generation rate. Such measurements and communication would give an effective control provided they operate rapidly compared with the time over which oxygen flux changes (eg, as cells pass the robots on millisecond timescales). Longer reaction times could lead to oscillations or chaotic behavior.[86]

A second approach to achieving a more uniform distribution of power is to space the robots at some distance from each other

on the vessel wall. This approach would be suitable if the aggregated robots do not need physical contact to achieve their task. For example, somewhat separating the robots would allow a relatively small number to span a distance along the vessel wall larger than the size of a single cell passing through the vessel. This aggregate would always have at least some robots between successive cells. Communicating sensor readings among the robots would then ensure the response (eg, releasing chemicals) is not affected by misleading sensor values due to the passage of a single cell, giving greater stability and reliability without the need for delaying response due to averaging over sensor readings as an alternative approach to accounting for passing cells. Another example for spaced robots is for directional acoustic communication, at distances of about 100 μm.[19] Achieving directional control requires acoustic sources extending over distances comparable with or larger than the sound wavelength. Plausible acoustic communication between nanorobots involves wavelengths of tens of micrometers.[19]

As a quantitative example of the benefit of spacing robots in the context of our axially symmetric model, we consider a set of rings of robots spaced apart along the vessel wall. When the distance between successive rings is sufficiently large, the power for each ring would be close to that of the isolated 1-μm ring given in Table 4. For example, the power for the low-demand scenario in the 1-μm ring of high-capacity robots decreases from 69 pW at high inlet concentration to 44 pW at low inlet concentration, which spans the range of power for a modest number of widely spaced 1-μm rings within a single vessel. As described in the section "Tissue power and heating," oxygen absorption by robots can affect concentration over a few tens of micrometers upstream of those robots. Thus, separating robot rings by, say, 100 μm will give power close to that of the isolated rings, with a gradual decrease in power for successive rings due to the decreasing cell saturation along the vessel.

A third approach to reducing variation in robot power, on average, is through changing pump rates in time. For example, adjacent nanorobot rings could operate with counterphased 50% duty cycles, with one ring and its second nearest neighbor ring using pumps while the intervening nearest neighbor has its pumps off and does not absorb oxygen. The alternating rings of robots would switch pumps on and off. In this case, robots would have larger power than seen in Figure 4 for the half of the time they are active and zero power for the other half. This temporal approach would not be suitable for tasks requiring all robots to have the same power simultaneously, but would be useful for tasks requiring higher burst power from robots throughout the aggregate where the robots are unable to store oxygen or power for later use. Provided the duty cycle is sufficiently long, our steady-state model can quantify the resulting power distribution. For example, in the low-demand scenario, total flux for the aggregate is 79% of that when every robot collects all the oxygen reaching its surface, and the minimum power per robot drops from 12 pW to 10 pW. Thus, when averaged over the duty cycle, this temporal technique reduces total power without benefiting the robots receiving the minimum power. In this case, the temporal approach does not improve minimum robot power (on average) as the power gain to a robot while its neighbors are off is less than a factor of 2, which does not compensate for the loss due

to each robot being off for half the time. Applying the steady-state model to this temporal variation in robot activity requires the duty cycle be long enough for the system to reach steady-state behavior after each switch between the active subset of robots, and that the switching time is short compared with the duty cycle so most of the robots' power arises during the steady-state portions of the cycle between switching. Diffusion provides one lower bound on this time: when neighboring robots switch pumps from on to off or vice versa, the characteristic diffusion time for oxygen over the distance between next nearest neighbors (1 μm) is about 0.1 millisecond. Adjustments in cell saturation for the 1-μm shift in the location of the active robots between each half of the duty cycle is a further limitation on the duty cycle time for the validity of the steady-state model, though this is likely to be minimal as the cells are separated from the robots by the plasma gap in the fluid. Because the steady-state model averages over the position of passing cells, another lower bound on the duty cycle arises from the time for a cell to pass the robots. From the speeds in Table 1, this time is at least 100 milliseconds.

Analytical model for an isolated spherical robot

The dependence of robot power on design parameters described above may appear contrary to simple intuitions. First, one might expect that the 10-μm ringset, with 10 times the surface area in contact with the plasma, would absorb about 10 times as much oxygen as the 1-μm ring. Instead we find only about a factor of 2 to 4 increase. Second, the benefit of pumps, less than a factor of 2 for the high-capacity robots, may seem surprisingly small. Third, the low-capacity robots, with 1/50th the reaction sites of the high-capacity robots, nevertheless generate about 1/5th as much power as high-capacity robots in the case with no pumps. And finally, in spite of the higher concentration near the robot surface than deep inside the robot when there are no pumps, increasing the reaction site density by placing all the reaction sites near the robot surface gives little benefit. Although the specific values of these designs depend on the geometry and environment used in our model, these general features of small robots obtaining power through diffusion apply in other situations as well.

In this section, we illustrate how these consequences of design choices arise in the context of a scenario for which the diffusion equation has a simple analytic solution, thereby identifying key physical effects leading to these behaviors. Specifically, we consider an isolated spherical robot of radius a in a stationary fluid with oxygen concentration C far from the sphere.

Such a sphere with a fully absorbing surface collects oxygen at a rate $4\pi D_{O_2} a C$.[69] This expression illustrates a key property of diffusive capture: The rate depends not on the object's surface area but on its size. This behavior, which also applies to other shapes,[69] arises because while larger objects have greater surface areas, they also encounter smaller concentration gradients. As a quantitative example, taking the sphere to have the same volume as the robot, that is, $(4/3)\pi a^3 = V_{robot}$ given in Table 3, the oxygen absorbed by the sphere generates 320 and 750 pW for C equal to the low and high inlet oxygen concentrations in the plasma from Table 1, respectively. These power values are larger than for robots on the vessel wall described above. Unlike the

sphere in a stationary fluid, the aggregated robots compete with each other for the oxygen, the fluid moves some of the oxygen past the robots before they have a chance to absorb it, and the surrounding tissue also consumes some of the oxygen. The replenishment of oxygen from the passing blood cells is not sufficient to counterbalance these effects.

The spherical robot also indicates the benefit of pumps. The fully absorbing sphere, with a zero concentration boundary condition at the surface, corresponds with using pumps. For robots without pumps, an approximation to Eq. (5) allows a simple solution. Specifically, because the Michaelis-Menten constant for the robot power generators, K, is much larger than the oxygen concentrations (eg, as seen in Figure 2), robot power generation from Eq. (5) is approximately $P_{robot} \approx (e\rho_{react}r / K)C_{o_2}$. Dividing by $e/6$ gives the oxygen consumption rate density as γC_{o_2}, where $\gamma = 6\rho_{react}r/K$. Solving the diffusion equation, Eq. (1), for a sphere in a stationary fluid with concentration C far from the sphere, with free diffusion through the sphere's surface and reaction rate density γC_{o_2} inside the sphere, gives the rate oxygen is absorbed by the sphere (and hence reacted to produce power) as[87] $4\pi D_{o_2}C(a - \mu\tanh(a/\mu))$ where $\mu = \sqrt{D_{o_2}/\gamma}$. Thus free diffusion produces a fraction

$$f_\mu = 1 - \frac{\mu}{a}\tanh\left(\frac{a}{\mu}\right) \qquad (10)$$

of the power produced by the fully absorbing sphere. The distance μ is roughly the average distance an oxygen molecule diffuses in the time a power-generation site consumes an oxygen molecule. When a freely diffusing molecule inside the robot has a high chance to diffuse out of the robot before it reacts (μ large compared with a), $f\mu$ is small so pumps provide a significant increase in power. Conversely, when μ is small compared with a, pumps provide little benefit: The large number of reaction sites ensure the robot consumes almost all the diffusing oxygen reaching its surface.

This argument illustrates a trade-off between using pumps to keep oxygen within the robot and the number of power generators. In particular, if internal reaction sites are easy to implement, then robots with many reaction sites and no pumps would be a reasonable design choice. Conversely, if reaction sites are difficult to implement while pumps are easy, then robots with pumps and few reaction sites would be a better choice.

A caveat for robots with few power-generating sites is that Eq. (10) applies when oxygen consumption is linear in the concentration, as given by γC_{o_2}. This expression allows arbitrarily increasing the reaction rate by increasing the concentration, no matter how small the number of reaction sites. This linearity is a good approximation of Eq. (5) only when $C_{o_2}K$. At larger concentrations, the power density saturates at $e\rho_{react}r$. When ρ_{react} is sufficiently small, this limit is below the power that could be produced from all the oxygen that a fully absorbing sphere collects. Thus, in practice, the benefit of using pumps estimated from the linear reaction rate, $G = f_\mu^{-1}$, is limited by this bound when ρ_{react} is small.

As an example, for a spherical robot with the high-capacity reaction site density of Table 3, $\gamma = 1.8 \times 10^4$/s and $\mu = 0.33$ μm, with the fairly modest benefit of pumps $G = 2.0$. The low-capacity robots have $\gamma = 360$/s and $\mu = 2.4$ μm with $G = 42$. In this case, the limit due to the maximum reaction rate of Eq. (5) applies, somewhat limiting the benefit of pumps to a factor of 34, but pumps still offer considerable benefit. These values for the benefits of pumps are somewhat larger than seen with our model for robots on the vessel wall. Nevertheless, the spherical example identifies the key physical properties influencing power generation with and without pumps and how they vary with robot design choices.

Eq. (10) also illustrates why power in the low-capacity robots is not as small as one might expect based on the reduction in reaction sites by a factor of 50. While the value of γ is proportional to ρ_{react}, the typical diffusion distance μ varies as $1/\sqrt{\rho_{react}}$, so a decrease in reaction sites by a factor of 50 only increases μ by about a factor of 7. The square root dependence arises from the fundamental property of diffusion: typical distance a diffusing particle travels grows only with the square root of the time. The modest change in diffusion distance, combined with Eq. (10), gives a smaller decrease in power than the factor of 50 decrease in capacity. The low-capacity robot has higher concentrations throughout the sphere, so each reaction site operates more rapidly than in the high-capacity case. This increase partially offsets the decrease in number of reaction sites.

Without pumps, the higher oxygen concentration near the sphere's surface than near its center means much of the power generation takes place close to the surface. Thus, we can expect an increase in power by placing reaction sites close to the surface rather than uniformly distributed throughout the sphere. Consistent with the results from the model described in the "Methods" section, evaluating Eq. (1) with the reaction confined to a spherical shell shows only a modest benefit compared with a uniform distribution. The benefit is larger for a thinner shell and is determined by the same ratio, a/μ, appearing in Eq. (10). In particular, the largest benefit of using a thin shell, only 12%, occurs for $a/\mu \approx 3.5$. The parameters for the high- and low-capacity robots are somewhat below this optimal value, giving only 10% and less than 1% benefit from a thin shell, respectively, for the sphere. These modest improvements correspond with the small benefits of using a thin shell seen in the solution to our model for both high- and low-capacity robots. Hence the solution of Eq. (1) for the sphere illustrates how, with a fixed number of reaction sites, concentrating them near the robot surface provides only limited benefit. The benefit of the higher reaction site density in the shell is almost entirely offset by the shorter distance molecules need to diffuse to escape from the thin reactive region. That is, the benefit of placing all the reaction sites in a thin shell arises from two competing effects. When μ is large (low capacity), the concentration is only slightly higher near the surface than well inside the sphere. So there is little benefit from placing the reaction sites closer to the surface. On the other hand, when μ is small (high capacity), even uniformly distributed reaction sites manage to consume most of the arriving oxygen, giving near-zero concentration at the surface of the sphere and little scope for further improvement by concentrating the reaction sites. Thus the largest, though still modest, benefit for a shell design is for intermediate values of a/μ.
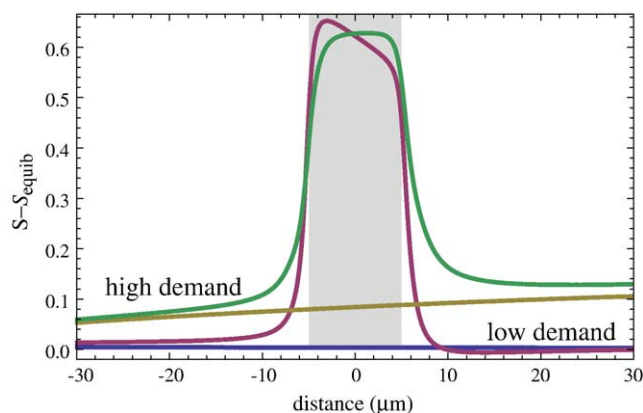
Figure 5. Deviation from equilibrium oxygen saturation in cells, $S - S_{equib}$, along the boundary between the cell and cell-free portions of the fluid illustrated in Figure 1, as a function of distance along that boundary. A deviation of zero indicates the oxygen held in the cells is in perfect equilibrium with the surrounding plasma. Saturation ranges between 0 and 1. The curves correspond with the low- and high-demand scenarios of Table 2, when robots are present (upper curves) or absent (lower curves). For the vessel without robots and low demand, $S - S_{equib}$ is indistinguishable from zero on the scale of the plot. The gray band indicates the 10-μm length of the vessel wall in which the robots are stationed, within the 60-μm length of the capillary illustrated.

Figure 6. Power density in tissue next to the vessel wall relative to maximum demand (ie, the ratio $P_{tissue} / P_{tissue}^{max}$ from Eq. (6)) as a function of position along the vessel. The curves are for the low- and high-demand scenarios of Table 2. The two lines at the top are for the vessel without robots, and the lower curves are for the 10-μm ringsets. In each case, the curve with higher values corresponds with the low-power demand scenario. The gray band indicates the 10-μm length of the vessel wall in which the robots has stationed, within the 60-μm length of the capillary illustrated.

Oxygen replenishment from passing cells

The high power density of the robots creates a steep gradient of oxygen concentration in the plasma. Thus, unlike the minor role for nonequilibrium oxygen release in tissue,[59] the small size of the robots makes passing red cells vary significantly from equilibrium with the concentration in the plasma. Figure 5 illustrates this behavior, using one measure of the amount of disequilibration: the difference between saturation S and the equilibrium value S_{equib} corresponding with the local concentration of oxygen in the plasma, as given by Eq. (2). We compare with a vessel without robots, in which the blood cells remain close to equilibrium.

Figure 5 shows that the kinetics of oxygen release from red cells plays an important role in limiting the oxygen available to the robots. However, the region of significant disequilibration is fairly small, extending only a few micrometers from the robots.

Tissue power and heating

The robots affect tissue power in two ways. First, the robots compete for oxygen with nearby tissue. Second, the robots consume oxygen from passing blood cells, thereby leaving less for tissue downstream of the robots.

For the effect on nearby tissue, Figure 6 shows how tissue power density varies next to the vessel wall. In the vessel without robots, power density declines slightly with distance along the vessel as the tissue consumes oxygen from the blood. The total reduction in tissue power density is fairly modest, less than 10% even for high power demand in the tissues. The relative reduction is less for tissue at larger distances from the vessel, though such tissue has lower power generation due to less oxygen reaching tissue far from the vessel. This reduction arises both from direct competition by the robots for available oxygen and the physical
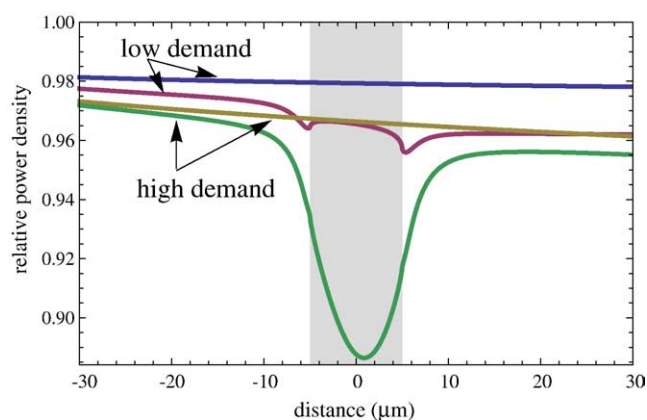
blockage of the capillary wall, forcing surrounding tissue to rely on oxygen diffusing a longer distance from unblocked sections of the wall. In the low-demand case, direct competition is the major factor, as seen by the dips in the power density at each end of the aggregate, where the absorbing flux is highest. In the high-demand case, the tissue's consumption reduces the amount of oxygen diffusing through the tissue on either side of the aggregate, giving the larger drop in tissue power density in the middle of the aggregate.

For longer-range consequences, Figure 7 shows how the oxygen saturation in the blood cells changes as they pass the robots. Slowly moving cells (in the low-demand scenario) are substantially depleted while passing the robots, even though tissue power demand in this scenario is low. This depletion arises from the cells remaining near the robots a relatively long time as cells move slowly with the fluid. The resulting saturation shown in the figure, around 0.6, is below the equilibrium saturation ($S = 0.7$) for typical concentrations at the venous end of capillaries, given in Table 1. Thus in the low-demand scenario, the robots remove more oxygen from passing cells than occurs during their full transit of a vessel containing no robots. In this scenario, the tissue has low power demand, so the depletion of oxygen from the cells may have limited effect on tissue along the vessel downstream of the robots. However, this reduction could significantly limit the number of robots that can be simultaneously present inside a given capillary.

Another observation from Figure 7 is a significant decrease in cell saturation a short distance upstream of the robots in the low-demand scenario. We can understand this behavior in terms of the Peclet number, which characterizes the relative importance of convection and diffusion over various distances.[65] In particular, D/v_{avg} is the distance at which diffusion and convection have about the same effect on mass transport in a moving fluid. At significantly longer distances, convection is the dominant effect, and absorption of oxygen at a given location in the vessel has
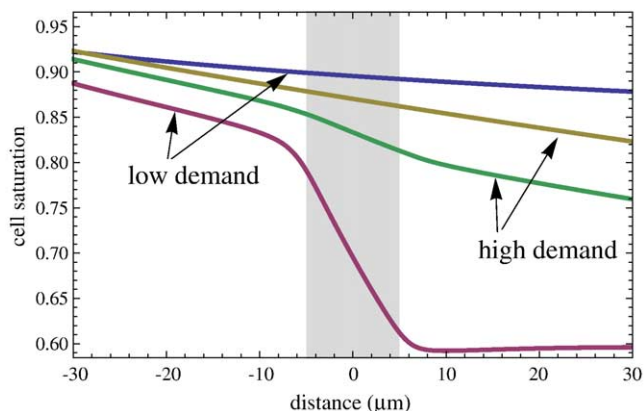
Figure 7. Cell saturation S as a function of distance along the vessel. Saturation ranges between 0 and 1. The curves correspond with the low- and high-demand scenarios of Table 2, with the upper curves of each pair corresponding with a vessel without robots. The gray band indicates the 10-μm length of the vessel wall in which the robots are stationed, within the 60-μm length of the capillary illustrated.

little effect on upstream concentrations over such distances. In our scenarios, D/v_{avg} ranges from ~2 μm (high demand) to ~10 μm (low demand). Thus, the robots significantly affect the oxygen concentration in the plasma over a few tens of micrometers upstream of their location. Cell saturation remains close to equilibrium in this upstream region (Figure 5), hence the reduced oxygen concentration in the plasma lowers cell saturation in this region upstream of the robots (Figure 7). This distance is also relevant for spacing rings of robots far enough apart to achieve nearly uniform power, as described in the section "Distribution of power among robots."

The devices in this example have a volume of $V_{robot} \approx 1$ μm³ so the robot power generation corresponds with power densities around 10^7 W/m³, several orders of magnitude larger than power densities in tissue, raising concerns of possible significant tissue heating by the robots. However, for the isolated aggregate used in this scenario, waste heat due to the robots' power generation is rapidly removed, resulting in negligible maximum temperature elevation of about 10^{-4}°C.

Fluid flow and forces on the robots

The robots change the fluid flow by constricting the vessel. With the same pressure difference as a vessel without robots, as used in our model, this constriction results in somewhat lower flow speed through the vessel. Specifically, the 1- and 10-μm-long aggregates reduce flow speed by 6% and 20%, respectively.

The fluid moving past the robots exerts a force on them. To remain on the wall, the robots must resist this force through their attachment to the vessel wall.[19] This force is a combination of pressure difference, between the upstream and downstream ends of the aggregate, and viscous drag. For the laminar flow, the force f is linear in the pressure gradient ∇p imposed on the vessel: $f = a\nabla p$ where $a = 1.56 \times 10^{-15}$ m³ and 5.02×10^{-16} m³ for the 10-μm and 1-μm ringsets, respectively. For example, the flow imposes a force of 160 pN on the 10-μm ringset when the pressure gradient is 10^5 Pa/m. The 10-μm

ringset experiences about three times the force of the 1-μm ring but covers 10 times the surface area. Thus, the larger aggregate requires about one-third the attachment force per robot. Applied forces can affect cells.[88] In particular, endothelial cells use forces as a trigger for new vessel growth,[89] which is important for modeling changes in the vessels over longer timescales than we consider in this article.[90]

Discussion

The scenarios of this article illustrate how various physical properties affect robot power generation. Robots about 1 μm in size positioned in rings on capillary walls could generate a few tens of picowatts in steady state from oxygen and glucose scavenged locally from the bloodstream. Aggregates can combine their oxygen intake for tasks requiring higher sustained power generation. The resulting high-power densities do not significantly heat the surrounding tissue but do introduce steep gradients in oxygen concentration due to the relatively slow reaction kinetics of oxygen release from red cells. The robots reduce oxygen concentration in nearby tissues, but generally not enough to significantly affect tissue power generation.

The fraction of the generated power available for useful activity within the robot depends on the efficiency of the glucose engine design, with ~50% a reasonable estimate for fuel cells.[19] The robots will have 5 to 30 pW of usable steady-state power while on the vessel wall. As one indication of the usefulness of this power for computation, current nanoscale electronics and sensors have an energy cost per logic operation or sensor switching event of a few hundred k_BT.[36] Though future technology should enable lower energy use,[19] even with 500 $k_BT \approx 2 \times 10^{-18}$ J the available power from circulating oxygen could support several million computational operations per second. At the size of these robots, significant movements of blood cells and chemical transport occur on millisecond timescales. Thus, the power could support thousands of computational operations (eg, for chemical pattern recognition) in this time frame. The aggregated robots could share sensor information and CPU cycles, thereby increasing this capability by a factor of tens to hundreds.

Devices of the type modeled in this article have numerous potential clinical applications. For example, nanorobot aggregates positioned in capillary beds will allow direct in situ detection of cancer biomarkers, including tumor cell membrane antigen signatures, tumor metabolic products, and blood-borne angiogenesis growth factors, enabling precise localization of early stage tumors and early detection of microtumors. The computational capability enabled by the fuel cell power could be used for chemical pattern recognition to enable precise long-term high-resolution chemical diagnostics because a fixed-site aggregate can monitor relevant low-concentration chemicals released near cells over extended periods of time to improve sensitivity to very low concentrations. Robot aggregates with available power of about 1000 pW could deliver precisely localized (ie, within about a single cell diameter) and precisely timed bursts (ie, within tens of milliseconds) of concentrated anticancer drug doses, providing minimal spillover to neighbor-

ing healthy cells and allowing amplification of the activity and effectiveness of co-delivered photodynamic, radiation, particle beam, or related cancer therapies. Nanorobot aggregates could serve as mobile (and perhaps switchable) contrast agents, enabling high-precision noninvasive capillary wall sampling and mapping thus enabling comprehensive in vivo clinical assays of capillary beds for sclerotic or necrotic vascular tissue and related vascular physiologic or structural pathologies. Nanorobot aggregates could pinpoint the location of bacterial metabolic products, allowing direct detection of biofilms and related focal infections. When infections are detected, the robot aggregates can dispense antibacterial agents with pinpoint accuracy allowing low-volume high-concentration aliquots to be employed therapeutically. Nanorobot aggregates could also perform functional metabolic monitoring of high-concentration metabolites in precisely localized capillary bed volumes in the brain over very narrow time intervals, greatly enhancing the spatial and time resolution of scans in small volumes compared with conventional positron emission tomography (PET) or functional MRI—a capability of clinical utility both for brain trauma assessment and for anesthesiology during surgery.

The robots need not generate power as fast as they receive oxygen, but could instead store oxygen received over time to enable bursts of activity as they detect events of interest. Robots with pumps have a significant advantage in burst-power applications because pumps enable long-term high-concentration onboard gas accumulation to support brief periods of near maximal power generation. As an example, in our scenarios individual robots with pumps receive about 10^8 molecule/s. If instead of using this oxygen for immediate power generation, the robot stored the oxygen received over 1 second, it would have enough to run the power generators at near maximal rate (giving about 10^4 pW) for several milliseconds. By contrast, robots without pumps would only have a modest benefit from oxygen diffusing into the robot, achieving a concentration equal to the ambient concentration in the surrounding plasma as given in Table 1. This concentration could only support generating several hundred picowatts for about a tenth of a millisecond. Thus, whereas pumps may give only modest improvement for steady-state power generation, they can significantly increase power available in short bursts.

Our model could be extended to estimate the amount of onboard storage that would be required to avoid pathologic conditions related to O_2 competition between tissues and nanorobots. In particular, larger aggregates would deplete oxygen over longer distances for which diffusion through the tissue from upstream of the robots would be insufficient. Furthermore, larger aggregates of tightly spaced robots would block transport from the capillary into the surrounding tissue even if the robots did not use much oxygen. Onboard oxygen storage would allow higher transient power densities for the robots, though this could lead to heating issues for larger aggregates. To estimate the potential for onboard storage, a ringset containing 200 robots with volume $200V_{robot} \approx 220$ μm³ of which 10% is devoted to compressed O_2 storage at 1000 atm at body temperature can store about 5×10^{11} molecules of O_2 in the aggregate. The incoming flow in the capillary provides about 0.2×10^{11} to 1×10^{11} molecules per second, depending on the

flow speed, of which about one-quarter to one-half is available to the tissue and robots. This means the oxygen stored in the aggregate is equivalent to only several seconds of oxygen delivery through the vessel. Thus, oxygen storage in the robots themselves cannot significantly increase mission duration, though such storage might be useful for short-term (ie, a few seconds) load leveling functions (eg, maintaining function during temporary capillary blockage due to white cell passage).

Alternatively, the aggregated robots could have oxygen supplemented with a modest circulating population of respirocytes[18] (ie, 1-μm spherical robots able to carry oxygen to tissues far more effectively than red blood cells). Such robots would continuously and entirely eliminate any oxygen depletion regions in the tissue due to robot power generation and allow higher robot power generation because oxygen would no longer be such a limiting factor. Such machines could not only carry significantly more oxygen than red blood cells but would also respond more quickly to abrupt decreases in partial pressure due to consumption by aggregated robots on vessel walls. For example, sensors should be able to detect the drop in concentration of the size we see near the robots—for example, 3×10^{22} to 2×10^{22} molecule/m³ (or about 40 to 20 mmHg)— within a millisecond.[19] This time is short enough that the machines will have moved only about a micrometer and so will still be near the robots. Once they detect the pressure drop, the machines could release oxygen rapidly, up to 1.5×10^8 molecule/s,[18] while passing near the aggregated robots. However, in practice the release rate is constrained by the effervescence limit in plasma to about 2.5×10^7 molecule/s.[19] An interesting question for future work is evaluating how much of this released oxygen reaches the robots on the vessel wall, which will depend on how close to the vessel wall the fluid places the respirocytes. In this situation, aggregated robots could also communicate[19] to passing respirocytes to activate or suppress their oxygen delivery, depending on the task at hand. Thus, both the oxygen handling capabilities of respirocytes, with faster kinetics and larger storage capacity than red cells, and the possibility of communication provide examples of the flexibility of small devices with programmable control. Moreover, this scenario illustrates the benefits of mixing robots with differing hardware capabilities.

Our model considers static aggregates on vessel walls but could be extended to study power availability for aggregates that move along the walls.[91] Another significant scenario is robots moving passively with the fluid, where they could draw oxygen from the surrounding plasma. The oxygen unloading model used here could evaluate how rapidly nearby cells would replenish oxygen in the plasma as the cells and robots move through the capillary.

We treat environmental parameters (eg, fluid flow speed and tissue oxygen demand) as fixed by the surroundings. Beyond the local changes in the robots' environment described by the model, sustained use of these robots could induce larger-scale responses. For example, the increased use of oxygen by the robots could lead to increased blood flow, as occurs with, say, exercising muscles, by increased pressure to drive the fluid at higher speed or dilation of the vessels. The local oxygen deficits due to high robot power use are smaller in scale than higher tissue demand

(eg, from increased activity in a muscle). Thus, an important open question is whether localized robot oxygen consumption over a long period of time can initiate a less localized response to increase flow in the vessels.

The possibility of large-scale responses to robot activity raises a broader issue for nanomedicine treatment design when technology allows altering the normal correlation among physical quantities used for signalling in the body.[19,20] An example at larger scales is the response to low oxygen mediated by excess carbon dioxide in the blood, which can lead to edema and other difficulties for people at high altitudes.[92] In terms of downstream consequences of the robots' oxygen use, low saturation of cells leaving an isolated capillary should not be a problem because the bulk of oxygen exchange occurs in the capillary bed, not in the larger collecting vessels. However, cells reaching low saturation before exiting the capillary would produce localized anoxia in the tissue near the end of the capillary. This could be relieved in part by oxygen diffusion from neighboring tissue cells if the anoxic region is not too large or too severe. Specific effects of such localized anoxia remain to be fully identified. Whole capillaries subjected to ischemic conditions over a period of days remodel themselves (eg, by adding new vascular branches and by increasing the tortuosity of existing vessels[93]). This observed behavior is likely to be a localized (ie, cell-level) response, hence we might expect such a response if a portion of a capillary downstream of the robots was driven into ischemic conditions. There could also be a localized inflammatory response to a large enough number of capillary-wall endothelial cells under stress, especially for cells stressed to the point of apoptosis, but moderate ischemia alone seems unlikely to generate this response.[94] Some chemicals, such as nitric oxide (NO), prostaglandin D2 (PGD2) and leukotriene D4 (LTD4), dilate the vessels. These chemicals can produce significant activity in the endothelial cells that line (and thus form the tube geometry of) the capillary vessel, so their influence can be fairly direct and quick.[95,96] Nanorobots in the vessels could release such chemicals to alter behavior of the vessels. Similarly, a large robot population constantly drawing excess oxygen supply could induce elevated erythropoietin secretion (if unregulated by the robots), increasing red cell production in the erythroid marrow.[18,97]

Direct heating is not a problem with aggregates of the size considered here, in spite of their high power density compared with tissue. For the large aggregate we examined (tightly covering 10 μm along the vessel wall), oxygen diffusion through the tissue from regions upstream and downstream of the robots provided oxygen to the tissue outside the section of the vessel blocked by the robots. Larger aggregates, especially if tightly packed, would significantly reduce oxygen in the tissues even if the robots used little power themselves, simply due to their covering the vessel wall over a long enough distance that diffusion through the tissue from unblocked regions is no longer effective. The inducement of nonlinear tissue thermal responses (eg, inflammation or fever) due to the heat generated by larger aggregates or multiple aggregates in nearby capillaries is an important question for future work.

Nanorobots parked or crawling along the luminal surface of the vessel may activate mechanosensory responses from the endothelial cells across whose surfaces the nanorobots touch.[40] If the aggregates cover a long section of the vessel wall, they could produce local edemas because narrowing of the vessels by the presence of the nanorobots increases local pressure gradients and fluid velocities. While we focus on a single aggregate in one microscopic vessel, additional issues arise if a large population of circulating robots forms many aggregates. In that case, the multiple aggregates will increase hydrodynamic resistance throughout the fluidic circuit. Thus, the robots could make the heart work slightly harder to pump fluid against the slightly higher load. Moreover, if robot aggregates detach from the wall without complete disaggregation, these smaller aggregates moving in the blood may be large enough to block a small vessel.

The scenarios examined in this article can suggest suitable controls to distribute power when robots aggregate. Moreover, power control decisions interact with the choices made for the aggregation process. For example, if the task requires a certain amount of total power for the aggregate (eg, as a computation hub), then the aggregation self-assembly protocol would depend on how much oxygen is available (eg, to make a larger aggregate in vessels with less available oxygen) or recruit more passing robots when the task needs more power. An example of this latter case could be if aggregates are used as computation hubs to validate responses to rare events: When local sensor readings indicate the possibility of such an event, the aggregate could temporarily recruit additional robots to increase power and computational capability for evaluating whether those readings warrant initiating treatment.

Another approach to designing controls for teams of robots is the formalism of partially observable Markov processes.[98,99] This formalism allows for arbitrarily complex computations among the robots to update their beliefs about their environment and other robots. Unfortunately, this generality leads to intractable computations for determining optimal control processes. For the situations we studied, the power constraints on capillary wall–resident microscopic robots operating with oxygen available in vivo means the local rules must be simple. Including this constraint in the formalism could allow it to identify feasible control choices for large aggregates of microscopic robots in these situations.

The power constraints from our model could provide useful parameters for less detailed models of the behavior of large numbers of robots in the circulation in the context of the scenarios examined in this article. In particular, power limits the computation, communication, and locomotion capabilities of the robots. These constraints could be incorporated in simplified models, such as cellular automata approaches to robot behavior. These automata are a set of simple machines, typically arranged on a regular lattice. Each machine is capable of communicating with its neighbors on the lattice and updates its internal state based on a simple rule. For example, a two-dimensional scenario shows how robots could assemble structures[100] using local rules. Such models can help understand structures formed at various scales through simple local rules and some random motions.[101,102] A related analysis technique considers swarms[103] (ie, groups of many simple machines or biological organisms such as ants). In these systems, individuals use simple rules to determine their behavior from information about a limited

portion of their environment and neighboring individuals. Typically, individuals in swarms are not constrained to have a fixed set of neighbors but instead continually change their neighbors as they move. Swarm models are well-suited to microscopic robots with their limited physical and computational capabilities and large numbers. Most swarm studies focus on macroscopic robots or behaviors in abstract spaces.[104] In spite of the simplified physics, these studies show how local interactions among robots lead to various collective behaviors[105] and provide broad design guidelines. A step toward more realistic, though still tractable, models of large aggregates could incorporate the power constraints from the model presented in this article.

In addition to evaluating performance of hypothetical medical nanorobots, theoretical studies identifying trade-offs between control complexity and hardware capabilities can aid future fabrication. One example is the design complexity of the robot's fuel acquisition and utilization systems. For steady-state operation on vessel walls, we found limited benefit of pumps over free diffusion when numerous onboard power generators can be employed. In such cases, our results indicate that a design without pumps does not sacrifice much performance. More generally, control can compensate for limited hardware (eg, sensor errors or power limitations), providing design freedom to simplify the hardware through additional control programs. Thus, the studies could help determine minimum hardware performance capabilities needed to provide robust systems-level behavior.

A key challenge for robot design studies based on approximate models is validating the results. In our case, the most significant approximations are the treatment of cells as an averaged component in the fluid and the lumped-model kinetics for oxygen unloading. With increased computational power, numerical solution of more accurate models could test the validity of these approximations. As technology advances to constructing early versions of microscopic robots, experimental evaluations will supplement theoretical studies. One such experiment is operating the robots in manufactured microfluidic channels.[65] This would test the robots' ability to aggregate at chemically defined locations and generate power reliably from known chemical concentrations in the fluid. After such in vitro experiments, early in vivo tests could involve robots acting as passive sensors in the circulatory system and aggregating at chemically distinctive locations. Such nanorobots will be useful not only as diagnostic tools and sophisticated extensions to drug delivery capabilities[106] but also as an aid to validate numerical models and hence develop robot designs and control methods for more active tasks.

References

1. Ishiyama K, Sendoh M, Arai KI. Magnetic micromachines for medical applications. J Magnetism Magn Mater 2002;242–245:41-6.
2. Mathieu JB, Martel S, Yahia L, Soulez G, Beaudoin G. Preliminary investigation of the feasibility of magnetic propulsion for future microdevices in blood vessels. Biomed Mater Eng 2002;15:367-74.
3. Martel S, Mathieu JB, Felfoul O, Chanu A, Aboussouan E, Tamaz S, et al. Automatic navigation of an untethered device in the artery of a living animal using a conventional clinical magnetic resonance imaging system. Appl Phys Lett 2007;114105:90.
4. Yesin KB, Exner P, Vollmers K, Nelson BJ. Design and control of in-vivo magnetic microrobots. In: Duncan JS, Gerig G, editors. Proceedings of the 8th international conference on medical image computing and computer-assisted intervention (MICCAI 2005). Berlin: Springer; 2005. p. 819-26.
5. Behkam B, Sitti M. Bacterial flagella-based propulsion and on/off motion control of microscale objects. Appl Phys Lett 2007;023902:90.
6. Cole E. Fantastic voyage: departure 2009. Wired 2007. Available at: http://222.wired.com/medtech/health/news/2007/01/72448. [Accessed 18 January 2007].
7. Morris K. Macrodoctor, come meet the nanodoctors. Lancet 2001;357:778.
8. NIH. National Institutes of Health Roadmap: Nanomedicine. Available at: nihroadmap.nih.gov/nanomedicine/index.asp; 2003.
9. Thomas TP, Shukla R, Majoros IJ, Myc A, Baker Jr JR. Polyamidoamine dendrimer-based multifunctional nanoparticles. In: Mirkin CA, Niemeyer CM, editors. Nanobiotechnology II: More concepts and applications. Hoboken, NJ: Wiley-VCH Press; 2007. p. 305-19.
10. Monroe D. Micromedicine to the rescue. Commun ACM 2009;52:13-5.
11. Popovtzer R, Agrawal A, Kotov NA, Popovtzer A, Balter J, Carey TE, et al. Targeted gold nanoparticles enable molecular CT imaging of cancer. Nano Lett 2008;8:4593-6.
12. Sershen S, Westcott S, Halas NJ, West J. Temperature-sensitive polymer-nanoshell composite for photothermally modulated drug delivery. J Biomed Mater Res 2000;51:293-8.
13. Vo-Dinh T, Kasili P, Wabuyele M. Nanoprobes and nanobiosensors for monitoring and imaging individual living cells. Nanomedicine: NBM 2006;2:22-30.
14. West JL, Halas NJ. Applications of nanotechnology to biotechnology. Curr Opin Biotechnol 2000;11:215-7.
15. Quintana A, Raczka E, Piehler L, Lee I, Myc A, Majoros I, et al. Design and function of a dendrimer-based therapeutic nanodevice targeted to tumor cells through the folate receptor. Pharm Res 2000;19:1310-6.
16. Baker JR, Quintana A, Piehler L, Banazak-Holl M, Tomalia D, Raczka E. The synthesis and testing of anti-cancer therapeutic nanodevices. Biomed Microdevices 2001;3:61-9.
17. Hessler TABJA, Mecke A, Banaszak-Holl M, Orr BG, Uppuluri S, Tomalia DA, et al. Tapping mode atomic force microscopy investigation of poly(amidoamine) core-shell tecto(dendrimers) using carbon nanoprobes. Langmuir 2002;18:3127-33.
18. Freitas Jr RA. Exploratory design in medical nanotechnology: a mechanical artificial red cell. Artif Cells Blood Substit Immobil Biotechnol 1998;26:411-30.
19. Freitas Jr RA. Nanomedicine. Vol. I: basic capabilities. Georgetown (Tex): Landes Bioscience; 1999. Available at: www.nanomedicine.com/NMI.htm.
20. Freitas Jr RA. Pharmacytes: an ideal vehicle for targeted drug delivery. J Nanosci Nanotechnol 2006;6:2769-75.
21. Martel S. The coming invasion of the medical nanorobots. Nanotechnol Perceptions 2007;3:165-73.
22. Hill C, Amodeo A, Joseph JV, Patel HRH. Nano- and microrobotics: how far is the reality? Expert Rev Anticancer Ther 2008;8:1891-7.
23. Win MN, Smolke CD. Higher-order cellular information processing with synthetic RNA devices. Science 2008;322:456-60.
24. Martel S, Felfoul O, Mohammadi M. Flagellated bacterial nanorobots for medical interventions in the human body. Proceedings of the 2nd IEEE conference on biomedical robotics and biomechatronics; 2008. p. 264-9.
25. Ferber D. Microbes made to order. Science 2004;303:158-61.
26. Andrianantoandro E, Basu S, Karig DK, Weiss R. Synthetic biology: new engineering rules for an emerging discipline. Mol Systems Biol 2006;2(msb4100073):E1-E14.

27. Benenson Y, Gil B, Ben-Dor U, Adar R, Shapiro E. An autonomous molecular computer for logical control of gene expression. Nature 2004;429:423-9.

28. Barreiro A, Rurali R, Harnandez ER, Moser J, Pichler T, Forro L, et al. Subnanometer motion of cargos driven by thermal gradients along carbon nanotubes. Science 2008;320:775-8.

29. Berna J, Leigh DA, Lubomska M, Mendoza SM, Perez EM, Rudolf P, et al. Macroscopic transport by synthetic molecular machines. Nat Mater 2005;4:704-10.

30. Collier CP, Wong EW, Belohradsky M, Raymo FM, Stoddart JF, Kuekes PJ, et al. Electronically configurable molecular-based logic gates. Science 1999;285:391-4.

31. Craighead HG. Nanoelectromechanical systems. Science 2000;290:1532-5.

32. Howard J. Molecular motors: structural adaptations to cellular functions. Nature 1997;389:561-7.

33. Fritz J, Baller MK, Lang HP, Rothuizen H, Vettiger P, Meyer E, et al. Translating biomolecular recognition into nanomechanics. Science 2000;288:316-8.

34. Marden JH, Allen LR. Molecules, muscles, and machines: universal performance characteristics of motors. Proc Natl Acad Sci U S A 2002;99:4161-6.

35. Montemagno C, Bachand G. Constructing nanomechanical devices powered by biomolecular motors. Nanotechnology 1999;10:225-31.

36. Wang SY, Williams RS, editors. Nanoelectronics, vol. 80. New York: Springer; 2005. Special issue of Applied Physics A.

37. Kufer SK, Puchner EM, Gumpp H, Liedl T, Gaub HE. Single-molecule cut-and-paste surface assembly. Science 2008;319:594-6.

38. Ager A. Inflammation: border crossings. Nature 2003;421:703-5.

39. Hogg T, Kuekes PJ. Mobile microscopic sensors for high-resolution in vivo diagnostics. Nanomedicine: NBM 2006;2:239-47.

40. Freitas Jr RA. Nanomedicine. Vol. IIA: biocompatibility. Georgetown (Tex): Landes Bioscience; 2003. Available at: www.nanomedicine.com/NMIIA.htm.

41. Vu TQ, Chowdhury S, Muni NJ, Qian H, Standaert RF, Pepperberg DR. Activation of membrane receptors by a neurotransmitter conjugate designed for surface attachment. Biomaterials 2005;26:1895-903.

42. Halloy J, Sempo G, Caprari G, Rivault C, Asadpour M, Tache F, et al. Social integration of robots into groups of cockroaches to control self-organized choices. Science 2007;318:1155-8.

43. Llinas RR, Walton KD, Nakao M, Hunter I, Anquetil PA. Neuro-vascular central nervous recording/stimulating system: using nanotechnology probes. J Nanoparticle Res 2005;7:111-27.

44. Freitas Jr RA. Clottocytes: artificial mechanical platelets. IMM Reports, 18. Palo Alto (Calif): Institute for Molecular Manufacturing; 2000. p. 9-11. Available at: http://www.imm.org/Reports/Rep018.html.

45. Leary SP, Liu CY, Apuzzo MLJ. Toward the emergence of nanoneurosurgery: part III—nanomedicine: targeted nanotherapy, nanosurgery, and progress toward the realization of nanoneurosurgery. Neurosurgery 2006;58:1009-26.

46. Hogg T. Distributed control of multiscale microscopic chemical sensor networks. J MicroNano Mechatronics 2008;4:168-77.

47. Sretavan D, Chang W, Keller C, Kliot M. Microscale surgery on axons for nerve injury treatment. Neurosurgery 2005;57:635-46.

48. Hogg T, Sretavan DW. Controlling tiny multi-scale robots for nerve repair. In: Veloso M, Kambhampati S, editors. Proceedings of the 20th national conference on artificial intelligence (AAAI2005). Menlo Park, CA: AAAI Press; 2005. p. 1286-91.

49. Mallouk TE, Sen A. Powering nanorobots. Sci Am 2009;300:72-7.

50. Soong RK, Bachand GD, Neves HP, Olkhovets AG, Craighead HG, Montemagno CD. Powering an inorganic nanodevice with a biomolecular motor. Science 2000;290:1555-8.

51. Wang X, Song J, Liu J, Wang ZL. Direct-current nanogenerator driven by ultrasonic waves. Science 2007;316:102-5.

52. Tucker R, Katira P, Hess H. Herding nanotransporters: localized activation via release and sequestration of control molecules. Nano Lett 2008;8:221-6.

53. Bechet D, Couleaud P, Frochot C, Viriot M-L, Guillemin F, Barberi-Heyob M. Nanoparticles as vehicles for delivery of photodynamic therapy agents. Trends Biotechnol 2008;26:612-21.

54. Chaudhuri SK, Lovley DR. Electricity generation by direct oxidation of glucose in mediatorless microbial fuel cells. Nat Biotechnol 2003;21:1229-32.

55. Logan BE, Murano C, Scott K, Gray ND, Head IM. Electricity generation from cysteine in a microbial fuel cell. Water Res 2005;39:942-52.

56. Malki M, De Lacey AL, Rodríguez N, Amils R, Fernandez VM. Preferential use of an anode as an electron acceptor by an acidophilic bacterium in the presence of oxygen. Appl Environ Microbiol 2008;74:4472-6.

57. Strang WG, Fix GJ. An analysis of the finite element method. Englewood Cliffs (NJ): Prentice-Hall; 1973.

58. McGuire BJ, Secomb TW. A theoretical model for oxygen transport in skeletal muscle under conditions of high oxygen demand. J Appl Physiol 2001;91:2255-65.

59. Popel AS. Theory of oxygen transport to tissue. Crit Rev Biomed Eng 1989;17:257-321.

60. Silver FH. Biological materials: structure, mechanical properties, and modeling of soft tissues. New York: New York University Press; 1987.

61. Purcell EM. Life at low Reynolds number. Am J Phys 1977;45:3-11.

62. Vogel S. Life in moving fluids. 2nd ed. Princeton (NJ): Princeton University Press; 1994.

63. Fung YC. Biomechanics: circulation. 2nd ed. New York: Springer; 1997.

64. Karniadakis G, Beskok A, Aluru N. Microflows and nanoflows: fundamentals and simulation. Berlin: Springer; 2005.

65. Squires TM, Quake SR. Microfluidics: fluid physics at the nanoliter scale. Rev Modern Phys 2005;77:977-1026.

66. Fetter AL, Walecka JD. Theoretical mechanics of particles and continua. New York: McGraw-Hill; 1980.

67. Pozrikidis C. Axisymmetric motion of a file of red blood cells through capillaries. Phys Fluids 2005;031503:17.

68. Berg HC, Purcell EM. Physics of chemoreception. Biophys J 1977;20:193-219.

69. Berg HC. Random walks in biology. 2nd ed. Princeton (NJ): Princeton University Press; 1993.

70. Mauroy B. Following red blood cells in a pulmonary capillary. ESAIM Proc 2008;23:48-65.

71. Clark Jr A, Federspiel WJ, Clark PA, Cokelet GR. Oxygen delivery from red cells. Biophys J 1985;47:171-81.

72. Geers C, Gros G. Carbon dioxide transport and carbonic anhydrase in blood and muscle. Physiol Rev 2000;80:681-715.

73. Briggs GE, Haldane JBS. A note on the kinetics of enzyme action. Biochem J 1925;19:338-9.

74. Keller KH. Effect of fluid shear on mass transport in flowing blood. Proceedings of the Federation of American Societies for Experimental Biology; 1971. p. 1591-9.

75. Secomb TW, Hsu R, Pries AR. Motion of red blood cells in a capillary with an endothelial surface layer: effect of flow velocity. Am J Physiol Heart Circ Physiol 2001;281:H629-36.

76. Hogg T. Modeling microscopic chemical sensors in capillaries. Open Nanomedicine J 2009;2:1-9.

77. Hernandez-Ortiz JP, Stoltz CG, Graham MD. Transport and collective dynamics in suspensions of confined swimming particles. Phys Rev Lett 2005;95:204501.

78. Riedel IH, Kruse K, Howard J. A self-organized vortex array of hydrodynamically entrained sperm cells. Science 2005;309:300-3.

79. Lerman K, Galstyan A, Martinoli A, Ijspeert AJ. A macroscopic analytical model of collaboration in distributed robotic systems. Artificial Life 2001;7:375-93.

80. Hogg T. Coordinating microscopic robots in viscous fluids. Autonomous Agents Multi-Agent Systems 2007;14:271-305.

81. Hamann H, Worn H, Crailsheim K, Schmickl T. Spatial macroscopic models of a bio-inspired robotic swarm algorithm. In: Chatila R, Merlet J-P, editors. Proceedings of the international conference on intelligent robots and systems (IROS 2008). Sophia-Antipolis, France: INRIA; 2008. p. 1415-20.

82. Vadapalli A, Goldman D, Popel AS. Calculations of oxygen transport by red blood cells and hemoglobin solutions in capillaries. Artif Cells Blood Substit Immobil Biotechnol 2002;30:157-88.

83. Bao J, Furumoto K, Fukunaga K, Nakao K. A kinetic study on air oxidation of glucose catalyzed by immobilized glucose oxidase for production of calcium gluconate. Biochem Eng J 2001;8:91-102.

84. COMSOL Group. Comsol multiphysics. Stockholm (Sweden): COMSOL Group; 2008. Available at: http://www.comsol.com/multiphysics.

85. Krogh A. The number and distribution of capillaries in muscles with calculations of the oxygen pressure head necessary for supplying the tissue. J Physiol 1919;52:409-15.

86. Hogg T, Huberman BA. Dynamics of large autonomous computational systems. In: Tumer K, Wolpert D, editors. Collectives and the design of complex systems. New York: Springer; 2004. p. 295-315.

87. Hogg T. Diffusion to a spherical reactor. The Wolfram Demonstrations Project. Available at: http://demonstrations.wolfram.com/DiffusionToASphericalReactor/2009.

88. Discher DE, Janmey P, Wang Y. Tissue cells feel and respond to the stiffness of their substrate. Science 2005;310:1139-43.

89. Deroanne CF, Lapiere CM, Nusgens BV. In vitro tubulogenesis of endothelial cells by relaxation of the coupling extracellular matrix-cytoskeleton. Cardiovasc Res 2001;49:647-58.

90. Szczerba D, Szekely G, Kurz H. A multiphysics model of capillary growth and remodeling. In: Alexandrov VN, van Albada GD, Sloot PMA, Dongarra J, editors. Proceedings of ICCS, part II. Berlin: Springer; 2006. p. 86-93.

91. Freitas Jr RA. The end of heart disease. Palo Alto (Calif): Institute for Molecular Manufacturing; 1996.

92. Schoene RB. Illnesses at high altitude. Chest 2008;134:402-16.

93. Bailey AM, O'Neill IV TJ, Morris CE, Peirce SM. Arteriolar remodeling following ischemic injury extends from capillary to large arteriole in the microcirculation. Microcirculation 2008;15:389-404.

94. Brown MD, Kent J, Kelsall CJ, Milkiewicz M, Hudlicka O. Remodeling in the microcirculation of rat skeletal muscle during chronic ischemia. Microcirculation 2003;10:179-91.

95. Soter NA, Lweis RA, Corey EJ, Austen KF. Local effects of synthetic leukotrienes (LTC4, LTD4, LTE4, and LTB4) in human skin. J Invest Dermatol 1983;80:115-9.

96. Sekar K. Inhaled nitric oxide in term and preterm infants. J Perinatol 2006;26:S4-7 [discussion S22–S23].

97. Erslev AJ, Beutler E. Production and destruction of erythrocytes. In: Beutler E, Lichtman M, Coller B, Kipps T, Seligsohn U, editors. Williams hematology. 5th ed. New York: McGraw-Hill; 1995. p. 425-41.

98. Cassandra AR, Kaelbling LP, Littman ML. Acting optimally in partially observable stochastic domains. Proceedings of the 12th National Conference on Artificial Intelligence (AAAI94). Menlo Park (Calif): AAAI Press; 1994. p. 1023-8.

99. Seuken S, Zilberstein S. Formal models and algorithms for decentralized decision making under uncertainty. Autonomous Agents Multi-Agent Systems 2008;17:190-250.

100. Arbuckle D, Requicha AAG. Active self-assembly. In: Tarn T-J, Fukuda T, editors. Proceedings of the IEEE International Conference on Robotics and Automation. Los Alamitos, CA: IEEE; 2004. p. 896-901.

101. Whitesides GM, Grzybowski B. Self-assembly at all scales. Science 2002;295:2418-21.

102. Griffith S, Goldwater D, Jacobson JM. Robotics: self-replication from random parts. Nature 2005;437:636.

103. Bonabeau E, Dorigo M, Theraulaz G. Swarm intelligence: from natural to artificial systems. Oxford: Oxford University Press; 1999.

104. Gazi V, Passino KM. Stability analysis of social foraging swarms. IEEE Trans Systems Man Cybernetics 2004;B34:539-57.

105. Vicsek T, Czirok A, Ben-Jacob E, Cohen I, Shochet O. Novel type of phase transition in a system of self-driven particles. Phys Rev Lett 1995;75:1226-9.

106. Allen TM, Cullis PR. Drug delivery systems: entering the mainstream. Science 2004;303:1818-22.